Highly-resolved large-eddy simulations of combustion stabilization in a scramjet engine model with cavity flameholder

Fábio Henrique Eugênio Ribeiro, Radouan Boukharfane, Arnaud Mura

To cite this version:

Fábio Henrique Eugênio Ribeiro, Radouan Boukharfane, Arnaud Mura. Highly-resolved large-eddy simulations of combustion stabilization in a scramjet engine model with cavity flameholder. Computers and Fluids, 2020, 197, pp.104344. 10.1016/j.compfluid.2019.104344 . hal-02358767

Highly-resolved large-eddy simulations of combustion stabilization in a scramjet engine model with cavity flameholder

Fábio Henrique Eugênio Ribeiro[a,b], Radouan Boukharfane[a,c], Arnaud Mura[a,*]

[a]*Institut Pprime UPR 3346 CNRS, ISAE ENSMA and University of Poitiers, France*
[b]*Instituto de Estudos Avançados, São José dos Campos, SP, Brasil*
[c]*Extreme Computing Research Center (ECRC), Computer Electrical and Mathematical Science and Engineering Division (CEMSE), KAUST, Thuwal, Saudi Arabia*

Abstract

Scramjet engines are high-speed airbreathing propulsion systems that do not require rotating elements to compress the air inlet stream. It is compressed dynamically through a supersonic intake system that is integrated in the forebody, thus leading to the required temperature and pressure levels for combustion to proceed within the combustor length. In such engines, the combustion chamber is crossed by a supersonic flow, which limits the time available to inject fuel, to mix it with oxidizer, to ignite the resulting mixture, and to reach complete combustion. Residence times can be increased thanks to cavities, which have the potential to stabilize combustion without excessive total pressure loss and are therefore used as flameholders in supersonic combustors. In the present study, we perform high-fidelity large-eddy simulations (LES) of a hydrogen jet in a supersonic crossflow (JISCF) of vitiated air, which is located upstream of a wall-mounted squared cavity. The performance of such high-fidelity LES does not only require the use of high-precision numerical schemes and reliable subgrid-scale models relevant to the so-called direct numerical simulation (DNS) limit, it is also strongly dependent on the mesh quality. Therefore, the present study places special emphasis on computational grid assessment through the introduction of a detailed numerical procedure, which aims at analysing mesh reliability. The corresponding procedure combines several verification subsets including (i) the inspection of distributions of the dimensions of the computational cells present at the wall location, (ii) the analysis of normalized velocity profiles and viscosity ratio in boundary layers, and (iii) the check of fields of some mesh quality indexes and associated distributions. For the geometry under consideration, it appears that the level of resolution imposed by a correct description of boundary layers leads to a mesh quality that is close to the one associated to DNS requirements. Combustion stabilization is then studied for two distinct values of the inlet vitiated airstream temperature. Two stabilization modes are recovered from the numerical simulations: cavity-stabilized and jet-wake stabilized regimes.

Keywords: High-speed flows, Large-eddy simulation (LES), Mesh reliability, Jet in supersonic crossflow (JISCF), Scramjet, Immersed boundary method (IBM)

---

[*] Corresponding author
Email address: `arnaud.mura@ensma.fr` (Arnaud Mura)

1. Introduction

Scramjet engine is a very promising propulsion strategy for hypersonic vehicles. Several fields of application, such as civil transport and launchers, are concerned. For access-to-space applications in particular, the use of airbreathing hypersonic propulsion systems could reduce significantly the launch costs. Preliminary studies showed remarkable and promising results in the use of this technology as a second stage of a three-stage-to-orbit launcher (Smart and Tetlow, 2009). Thus, there is a special interest in the hypersonic vehicle as the promise of an airbreathing reusable system able to lift payloads into Earth orbit.

One of the main advantages of scramjets over concurrent technologies is related to the fact that it does not carry oxidizer, which is scooped directly from the atmosphere, thus providing a considerable weight reduction and allowing for higher payloads and specific impulses compared to standard rocket engines (Heiser and Pratt, 1994; Smart, 2008; Segal, 2009). This also means reduced costs, reduced complexity, and also lighter ground support. However, high-speed flights in the atmosphere raise several specific issues related, among others, to aerodynamic heating and vehicle drag, which impose the cooling of both the vehicle and the engine for prolonged operations. The corresponding high temperature levels also contribute to the dissociation of molecules, e.g. oxygen and nitrogen molecules decompose and recombine, and they may even ionize at higher speeds (Anderson, 1989; Segal, 2009). Since it produces no thrust at zero flight speed, such an engine must be ignited after it has been accelerated to its takeover speed thanks to a secondary propulsion system. The issues associated to ignition and propulsion efficiency during this takeover stage are thus important in the scramjet development but they lie outside the scope of the present study, which is concerned with combustion stabilization, once significant flight Mach number values are reached.

As emphasized above, there are several possible applications of scramjet engines, including civil high-speed aircrafts, space exploration as reusable stages for access to Earth orbit, and military hypersonic weapons (Urzay, 2018). Despite many impressive achievements obtained in the field since the early sixties, still today there are no scramjet engines being used in practical devices: many developments including experimental flights and ground-based testings are currently in progress. In such engines, the combustion chamber is crossed by a supersonic flow, which limits considerably the time available to inject fuel, mix it with the oxidizer, ignite the resulting mixture, and stabilize combustion. Combustion ignition and stabilization indeed appears as one of the most challenging issues (Cai et al., 2018). One promising solution is the wall-mounted cavity, which has been shown to be quite efficient in stabilizing combustion without excessive total pressure loss (Ben-Yakar and Hanson, 2001; Mathur et al., 2001; Gruber et al., 2004). The recirculation zones that develop inside the cavity increase the residence time of intermediate combustion products that can continuously initiate chemical reactions. However, the understanding of the interaction of the fuel jet with the wall-mounted cavity is far from being an easy task (Cai et al., 2016; Gong et al., 2017) and it has motivated a large amount of experimental studies in both reactive and non-reactive conditions. For instance, Ben-Yakar and Hanson (2001) investigated hydrogen normal injection in air cross-flow upstream of a cavity simulating Mach 10 flight conditions. High-speed Schlieren visualization and planar laser-induced fluorescence (OH-PLIF) were used to characterize the compressible flow topology and combustion development. The first OH fluorescence events are found to take place in the recirculation zone upstream of the underexpanded jet and the signal of fluorescence extends further downstream along the outer edge of the jet. Micka and Driscoll (2008) studied the combustion characteristics of a dual-mode scramjet combustor with normal fuel injection upstream of a cavity flame-holder. Depending on the value of the vitiated airstream stagnation temperature, combustion is either anchored at the cavity leading edge and spreads into the main flow at an approximately constant angle (low stagnation temperature levels) or stabilizes a short distance downstream of the hydrogen injection, in its wake, and features a curved leading edge (high stagnation temperature levels). The combustion stabilization is analysed on the basis of premixed flame propagation and the possibility that it flashes forward to a relatively stable location in the hydrogen jet-wake. Sun et al. (2008) also analysed combustion in a supersonic combustor with normal hydrogen injection upstream of cavity flame-holders. Their investigation is based on the combination of experimental observations using OH-PLIF and numerical simulations performed within a hybrid RANS/LES framework. It is shown that an approximately steady flame may be maintained in the cavity shear layer. Hot combustion products can be transported towards the jet inlet stream through a process of interaction between the counter-rotating vortices issued from the jet and the cavity shear layer.

In the present study, it is attempted to perform high-fidelity numerical simulations of a scramjet model representative of experimental investigations previously conducted at the University of Michigan (Micka and Driscoll, 2009; Micka, 2010). In the experiments under consideration, a sonic jet of hydrogen is injected into a supersonic crossflow of vitiated air upstream of a wall-mounted cavity. The computations are performed with the high-performance computational solver `CREAMS` (Martínez-Ferrer et al., 2014, 2017a) that has been developed to perform the numerical simulation of compressible reactive multi-component flows on massively-parallel architectures. The solver makes use of high-order precision numerical schemes applied on structured meshes. The simplified computational geometry consists of a constant section channel, followed by the wall-mounted cavity section, and finally the diverging section. This geometry is handled thanks to the recent immersed boundary method (IBM) introduced by Boukharfane et al. (2018). The corresponding set of computations is expected to be useful to analyse the reactive flow topology and structure as well as combustion regimes, which can be investigated on the basis of standard turbulent combustion diagrams. Combustion stabilization is studied for two distinct values of the inlet vitiated air-stream temperature, which are denoted RFSC-LST and RFSC-HST, for low- and high-stagnation temperature levels, respectively. A preliminary inspection of numerical data confirms that two stabilization modes can be observed: cavity stabilization mode for case RFSC-LST and jet-wake stabilization mode for case RFSC-HST.

The present manuscript is organized as follows, in section 2, the large-eddy simulation model and numerical methods are presented. It is followed by a short section where the computational setup is set forth. This section includes the presentation of the computational domain, its discretization, and associated boundary conditions. The next part of the manuscript, section 4, provides a detailed analysis of computational resolution issues. Finally, some results of both non-reactive and reactive flow simulations are discussed in section 5. The manuscript ends with a brief conclusion section 6, where some perspectives for future works are also presented.

2. Governing equations and numerical methods

The present study is conducted within the large-eddy simulation (LES) framework, i.e., the largest scales of the flow are explicitly computed, while the subgrid-scale (SGS) effects, resulting from the smallest ones, are modelled. Thus, the following set of filtered transport equations, written in a conservative form, is used to describe the multicomponent reactive flowfield

$$\frac{\partial \overline{\rho}}{\partial t} + \frac{\partial \overline{\rho}\widetilde{u}_i}{\partial x_i} = 0 \tag{1}$$

$$\frac{\partial \overline{\rho}\widetilde{u}_j}{\partial t} + \frac{\partial \overline{\rho}\widetilde{u}_i\widetilde{u}_j}{\partial x_i} = -\frac{\partial \overline{p}}{\partial x_j} + \frac{\partial \overline{\tau}_{ij}}{\partial x_i} - \frac{\partial}{\partial x_i}\left(\overline{\rho u_i u_j} - \overline{\rho}\widetilde{u}_i\widetilde{u}_j\right) \tag{2}$$

$$\frac{\partial \overline{\rho}\widetilde{e}_t}{\partial t} + \frac{\partial \overline{\rho}\widetilde{u}_i\widetilde{e}_t}{\partial x_i} = -\frac{\partial \overline{p}\widetilde{u}_i}{\partial x_i} + \frac{\partial \widetilde{u}_i\overline{\tau}_{ij}}{\partial x_j} - \frac{\partial \overline{\mathcal{J}}_i}{\partial x_i} - \frac{\partial}{\partial x_i}\left(\overline{(\rho e_t + p)u_i} - (\overline{\rho}\widetilde{e}_t + \overline{p})\widetilde{u}_i\right) \tag{3}$$

$$\frac{\partial \overline{\rho}\widetilde{Y}_\alpha}{\partial t} + \frac{\partial \overline{\rho}\widetilde{u}_i\widetilde{Y}_\alpha}{\partial x_i} = -\frac{\partial \overline{\rho Y_\alpha V_{\alpha i}}}{\partial x_i} - \frac{\partial}{\partial x_i}\left(\overline{\rho Y_\alpha u_i} - \overline{\rho}\widetilde{Y}_\alpha\widetilde{u}_i\right) + \overline{\rho}\widetilde{\dot{\omega}}_\alpha \tag{4}$$

where t denotes time, x_i is the Cartesian coordinate in direction i (with $i = 1, \ldots, 3$), u_i is the velocity component in the same direction, ρ is the density, p is the pressure, $e_t = e + u_i u_i/2$ is the total specific energy which is obtained as the sum of the kinetic energy and internal specific energy e, and finally Y_α is the mass fraction of chemical species α (with $\alpha = 1, \ldots, \mathcal{N}_{\mathrm{sp}}$). The integer $\mathcal{N}_{\mathrm{sp}}$ denotes the number of chemical species. In the above equations, $\overline{\Phi}$ is the filtered value of any quantity Φ, while $\widetilde{\Phi}$ denotes its density-weighted or Favre filtered counterpart: $\widetilde{\Phi} = \overline{\rho\Phi}/\overline{\rho}$. The thermodynamic variables are interrelated through the filtered pressure field $\overline{p} = \overline{\rho}\mathcal{R}\widetilde{T}/\widetilde{\mathcal{W}}$ with $\mathcal{R}$ the universal gas constant, T the temperature, and $\widetilde{\mathcal{W}}^{-1} = \sum_{\alpha=1}^{\mathcal{N}_{\mathrm{sp}}} \widetilde{Y}_\alpha/\mathcal{W}_\alpha$ the molar weight of the multicomponent mixture ($\mathcal{W}_\alpha$ being the molar weight of species α). In Eq. (4), the quantities $V_{\alpha i}$ and $\dot{\omega}_\alpha$ denote the diffusion velocity and chemical production rate of species α, respectively. The filtered stress tensor is evaluated from $\overline{\tau}_{ij} = 2\widetilde{\mu}(\widetilde{S}_{ij} - \widetilde{S}_{kk}\delta_{ij}/3)$ with $\widetilde{S}_{ij} = \left(\partial\widetilde{u}_i/\partial x_j + \partial\widetilde{u}_i/\partial x_j\right)/2$ denoting the resolved strain-rate tensor. It is noteworthy that the retained system of filtered equations is similar to the one previously considered by Ragab et al. (1992), Piomelli (1999), Kosovic et al. (2002), and Dubois et al. (2002).

For the present set of numerical simulations, standard modelling assumptions are retained. A mixture-average formulation is used to describe multicomponent molecular diffusion (Hirschfelder and Curtiss, 1949). Moreover, it is assumed that the filtered molecular diffusion fluxes and filtered heat flux can be deduced from their instantaneous expressions, but applied to filtered quantities. The components of the filtered molecular diffusion flux of chemical species α are thus approximated from

$$\overline{\rho Y_\alpha V_{\alpha i}} = -\overline{\rho}\widetilde{D}^m_\alpha \frac{\mathcal{W}_\alpha}{\widetilde{\mathcal{W}}}\frac{\partial \widetilde{X}_\alpha}{\partial x_i} + \overline{\rho}\widetilde{Y}_\alpha \widetilde{V}^c_i \tag{5}$$

where X_α denotes the molar fraction of species α and $\widetilde{D}^m_\alpha$ is the matrix of the diffusion flux coefficients of the same chemical species. It is worth noting that the last term of Eq. (5) is a correction term used to enforce total mass conservation. Indeed, at each time step, each component of the correction velocity $\widetilde{V}^c_i = \sum_{\beta=1}^{\mathcal{N}_{\mathrm{sp}}} \widetilde{D}^m_\beta (\mathcal{W}_\beta/\widetilde{\mathcal{W}})\partial\widetilde{X}_\beta/\partial x_i$ is evaluated and added to the filtered velocity component $\widetilde{u}_i$ so as to enforce compatibility between the discrete forms of total mass and species mass fractions conservation equations.

The i-component of the filtered molecular heat flux is expressed as follows:

$$\overline{\mathcal{J}}_i = -\widetilde{\lambda}\frac{\partial \widetilde{T}}{\partial x_i} + \sum_{\alpha=1}^{\mathcal{N}_{\mathrm{sp}}} \overline{\rho}\,\widetilde{Y}_\alpha\,\widetilde{V}_{\alpha i}\,\widetilde{h}_\alpha \tag{6}$$

where $\widetilde{\lambda}$ is the thermal conductivity of the multicomponent mixture as evaluated from the filtered composition.

The subgrid-scale (SGS) stress tensor $T_{ij} = \overline{\rho u_i u_j} - \overline{\rho}\widetilde{u}_i\widetilde{u}_j$ is modelled within the Boussinesq's framework. Its deviatoric part is thus evaluated from $T_{ij} - T_{kk}\delta_{ij}/3 = -2\mu_{\mathsf{SGS}}(\widetilde{S}_{ij} - \widetilde{S}_{kk}\delta_{ij}/3)$, where $\mu_{\mathsf{SGS}} = \overline{\rho}\,\nu_{\mathsf{SGS}}$ is the SGS eddy viscosity and T_{kk} denotes the isotropic contribution. The closure of the SGS mass fluxes relies on the standard turbulent diffusivity assumption, which may be expressed in the following general form:

$$T_{\varphi,i} = \overline{\rho\varphi u_i} - \overline{\rho}\widetilde{\varphi}\widetilde{u}_i = \overline{\rho}\left(\widetilde{\varphi u_i} - \widetilde{\varphi}\widetilde{u}_i\right) = -\overline{\rho}D_{\mathsf{SGS}}\frac{\partial\widetilde{\varphi}}{\partial x_i} \tag{7}$$

where φ denotes any scalar quantity, $D_{\mathsf{SGS}} = \nu_{\mathsf{SGS}}/\mathrm{Sc}_{\mathsf{SGS}}$ is the turbulent diffusivity and $\mathrm{Sc}_{\mathsf{SGS}}$ corresponds to the SGS turbulent Schmidt number, the value of which is set to 0.7. Finally, the last term of the filtered energy equation, see Eq. (3), may be rewritten as follows:

$$\overline{(\rho e_t + p)u_j} - (\overline{\rho}\widetilde{e}_t + \overline{p})\widetilde{u}_j = \underbrace{\left[\overline{\rho c_p T u_j} - \overline{\rho}\,\overline{c_p}\widetilde{T}\widetilde{u}_j\right]}_{\mathcal{Q}_j} + \underbrace{\left[\frac{1}{2}\left(\overline{\rho u_i u_i u_j} - \overline{\rho}\widetilde{u}_i\widetilde{u}_i\widetilde{u}_j\right)\right]}_{\psi_{iij}} - \frac{1}{2}T_{ii}\widetilde{u}_j \tag{8}$$

where $\mathcal{Q}_j = -\lambda_{\mathsf{SGS}}\partial\widetilde{T}/\partial x_j$ is nothing but the SGS heat flux also modelled using the gradient-diffusion approximation, with $\lambda_{\mathsf{SGS}} = \mu_{\mathsf{SGS}}\overline{c_p}/\mathrm{Pr}_{\mathsf{SGS}}$ the turbulent thermal conductivity and $\mathrm{Pr}_{\mathsf{SGS}}$ the SGS turbulent Prandtl number. The value of $\mathrm{Pr}_{\mathsf{SGS}}$ is set to 0.7. In Eq. (8), the quantity ψ_{ijk} denotes the triple velocity correlation tensor, which is closed by retaining the Daly and Harlow expression $\psi_{ijk} = C_{c3}\nu_{\mathsf{SGS}}\partial T_{ij}/\partial x_k$ with $C_{c3} = 0.08$ (Daly and Harlow, 1970). At this level, it must be precised that the SGS eddy viscosity μ_{SGS} is evaluated from the wall-adapting local eddy (WALE) model of Nicoud and Ducros (1999):

$$\mu_{\mathsf{SGS}} = \overline{\rho}(C_w\Delta)^2\frac{(S^d_{ij}S^d_{ij})^{3/2}}{(\widetilde{S}_{ij}\widetilde{S}_{ij})^{5/2} + (S^d_{ij}S^d_{ij})^{5/4}} \tag{9}$$

where $C_w = C_s\sqrt{10.6}$ is the WALE model constant, $\Delta = (\Delta x_1 \Delta x_2 \Delta x_3)^{1/3}$ is the characteristic mesh size, and S^d_{ij} is the traceless symmetric part of the square of the resolved velocity gradient tensor:

$$S^d_{ij} = \frac{1}{2}\left(\frac{\partial \widetilde{u}_i}{\partial x_l}\frac{\partial \widetilde{u}_l}{\partial x_j} + \frac{\partial \widetilde{u}_j}{\partial x_l}\frac{\partial \widetilde{u}_l}{\partial x_i}\right) - \frac{1}{3}\frac{\partial \widetilde{u}_m}{\partial x_l}\frac{\partial \widetilde{u}_l}{\partial x_m}\delta_{ij} \tag{10}$$

The following set of computations have been performed with C_s set to its standard value $C_s = 0.18$. In this respect, it should be emphasized that the present closure of the filtered Navier-Stokes equations gathers the same modelling ingredients as those previously retained by Techer et al. (2018). Finally, the filtered chemical rates $\widetilde{\dot{\omega}}_\alpha$ that appear in the right-hand-side of the filtered species mass fraction transport equations are represented using either the perfectly stirred reactor (PSR) or the unsteady partially stirred reactor (U-PaSR) closure (Berglund et al., 2010; Moule et al., 2014a). These two SGS closures make use of a detailed description of chemistry and the mechanism of O'Conaire et al. (2004), consisting of 9 chemical species (H_2, O_2, H_2O, H, O, OH, HO_2, H_2O_2 and N_2) and 21 elementary reaction steps, is used to represent H_2-air chemistry. Additional details about these two SGS turbulent combustion closures will be provided in the next sections of the manuscript.

Computations are performed with the computational fluid dynamics (CFD) solver `CREAMS`. The reader is referred to Martínez-Ferrer et al. (2014) and to Boukharfane et al. (2018) for an exhaustive presentation of this solver including its application to a large number of verification test cases. Its main features are as follows: the treatment of the inviscid component of the transport equations relies on a seventh-order accurate weighted essentially non-oscillatory (WENO7) reconstruction of the characteristic fluxes. In practice, the numerical solver uses a high-order accuracy finite difference scheme, and the application of the nonlinear weighting procedure of the WENO7 scheme is conditioned to a shock sensor that involves the local values of the normalized spatial variations of both pressure and density (Buttay et al., 2016). The viscous and molecular diffusion fluxes are evaluated thanks to an eighth-order centered finite difference scheme. The temporal integration is performed using a third-order Runge-Kutta algorithm. Finally, the present set of computations makes use of a recent immersed boundary method (IBM) to describe the wall-mounted cavity. The corresponding IBM strategy combines direct-forcing (DF) and ghost-point-forcing (GPF) algorithms (Boukharfane et al., 2018).

3. Computational setup

Figure 1 displays the supersonic combustion facility studied at the University of Michigan. It consists of a two-dimensional Mach 2.2 nozzle, a constant area isolator that extends over 400.0 mm up to the leading edge of a rectangular cavity, which is followed by a 349.0 mm long and 4 degree diverging section dumping into a 152.0 mm diameter exhaust. The cavity spans the entire width of the test section, which is equal to 38.1 mm. It is 50.8 mm long and 12.7 mm high, thus featuring a rather small length to depth ratio ($l_2/h_2 \leq 10.0$) in such a manner that it can be considered as an open cavity (Lawson and Barakos, 2011). Upstream of this wall-mounted cavity, a sonic hydrogen jet is injected into the vitiated air supersonic crossflow .

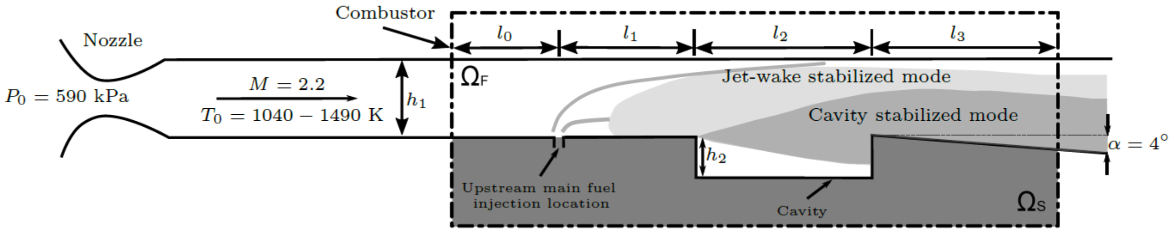

Figure 1: Schematics of the combustion facility with the computational domain highlighted

The computational domain, highlighted in Fig. 1, is restricted to the consideration of the transverse jet and cavity flowfield. It can be decomposed into three distinct parts: a constant section channel s_1 with length $L_{x_1,s_1} = l_0 + l_1 = 94.5$ mm and height $L_{x_2,s_1} = h_1 = 39.4$ mm, a section s_2 with length $L_{x_1,s_2} = l_2 = 50.8$ mm featuring the wall-mounted cavity with depth $h_2 = 12.7$ mm, and a four-degree diverging section s_3 with length $L_{x_1,s_3} = l_3 = 76.2$ mm. The total length of the computational domain is thus $L_{x_1} = 221.5$ mm and it is $L_{x_3} = 38.1$ mm in the spanwise direction. Section s_1 features the hydrogen injection port with diameter $D_1 = 2.5$ mm located along the combustor centerline at 44.5 mm upstream of the cavity leading edge.

The corresponding computational grid features approximately $42,000,000$ points and it is refined at some locations including the vicinity of walls, the hydrogen jet exit, and the shear layer that develops above the cavity. The characteristic dimensions of the resulting computational grid elements remain bounded between 15 μm and 275 μm, see Table 1.

	Δx_1 (m)	Δx_2 (m)	Δx_3 (m)
Min value	$5.0 \cdot 10^{-5}$	$1.5 \cdot 10^{-5}$	$5.0 \cdot 10^{-5}$
Max value	$1.475 \cdot 10^{-3}$	$4.062 \cdot 10^{-4}$	$2.478 \cdot 10^{-4}$
Average value	$2.711 \cdot 10^{-4}$	$2.387 \cdot 10^{-4}$	$1.865 \cdot 10^{-4}$

Table 1: Characteristic dimensions of the computational grid

A normalized mesh concentration parameter Δx_i^* is introduced to follow the spatial discretization evolution with respect to its smallest and largest characteristic dimensions along each of the three directions. It is evaluated from $\Delta x_i^* = (\Delta x_{i,max} - \Delta x_i)/(\Delta x_{i,max} - \Delta x_{i,min})$, where Δx_i^* is the mesh concentration parameter, Δx_i the current (i.e., local) computational grid size, $\Delta x_{i,min}$ its smallest value, and $\Delta x_{i,max}$ its largest value. Thus, the value of Δx_i^* ranges between zero, for small concentration of computational nodes (i.e., large characteristic mesh dimension), and unity, for high concentration of computational nodes (i.e., small characteristic mesh dimension). Figure 2 reports the normalized mesh concentration Δx_1^*, Δx_2^*, and Δx_3^* along the three spatial directions. It is noteworthy that the mesh origin has been set at the center of the fuel injection exit diameter. The bottom wall, including the wall-mounted cavity geometry, is modelled using the IBM. Except for the fuel inlet boundary condition (BC), which is set as a supersonic inlet BC, the corresponding boundary condition is processed as a solid (i.e., impermeable) adiabatic wall with the energy and scalar zero-flux Neumann boundary conditions imposed using the GPF framework, and the zero-velocity Dirichlet boundary condition (i.e., no-slip wall) imposed through the combined GPF-DF framework, see Boukharfane et al. (2018) for further details. On the left side of the computational domain, the vitiated air inlet boundary condition is set as a supersonic inlet BC. The lateral and top boundaries are processed as slip walls. Finally, on the right side of the computational domain, the supersonic outlet is processed using extrapolation together with an additional sponge region combining both grid coarsening and explicit filtering, thus following the strategy previously retained by Buttay et al. (2016, 2017). Further details about the fuel and vitiated air inlet conditions are provided below.

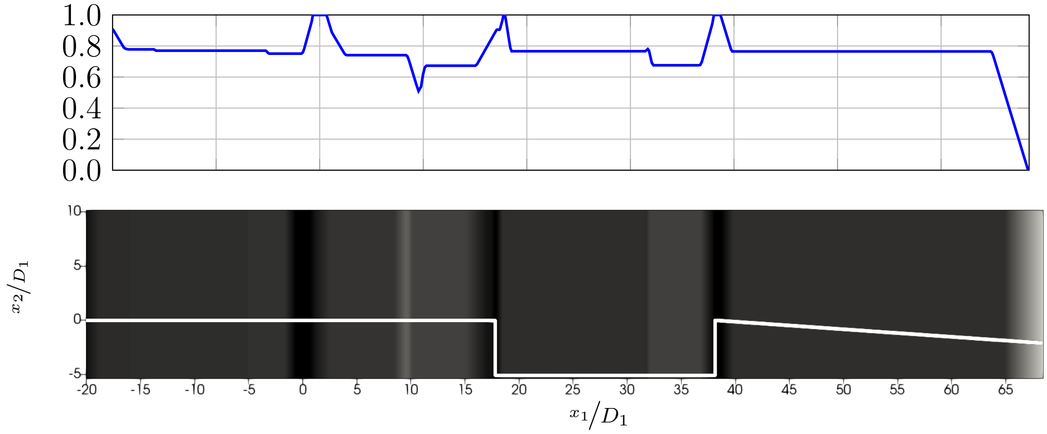

(a) Δx_1 (obtained at $x_3/D_1 = 0.0$)

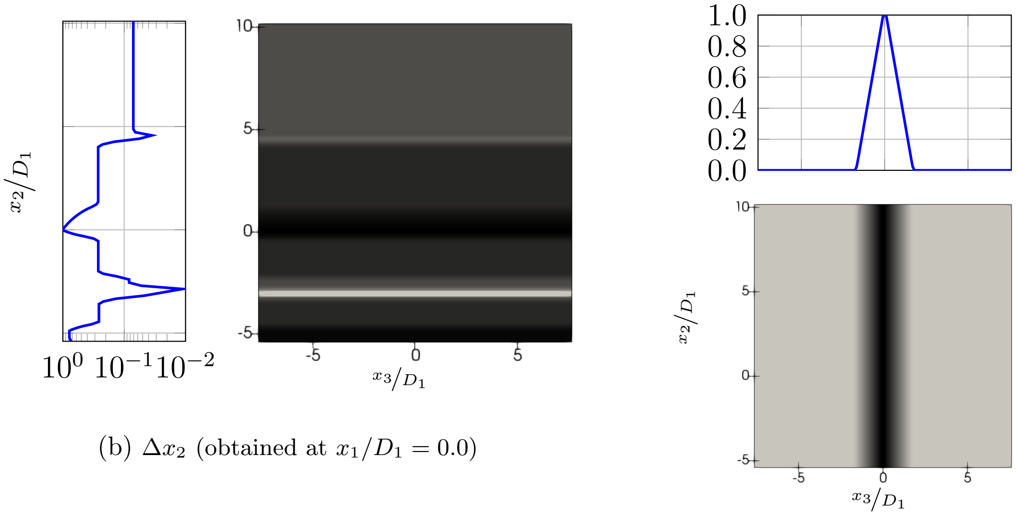

(b) Δx_2 (obtained at $x_1/D_1 = 0.0$)

(c) Δx_3 (obtained at $x_1/D_1 = 0.0$)

Figure 2: Normalized mesh size distributions with the cavity geometry delineated with a white line

	case RFSC-LST		case RFSC-HST	
	fuel	vitiated air	fuel	vitiated air
$p\,(\mathrm{kPa})$	845.0	55.410	755.0	55.426
$Y_{\mathrm{H_2}}$	1.0	0.0	1.0	0.0
$Y_{\mathrm{O_2}}$	0.0	0.244	0.0	0.251
$Y_{\mathrm{N_2}}$	0.0	0.671	0.0	0.607
$Y_{\mathrm{H_2O}}$	0.0	0.085	0.0	0.142

Table 2: Hydrogen and vitiated air inlets characteristics

The initial air stagnation (i.e., total) pressure is $p_{t,0} = 590.0$ kPa and two distinct values of the vitiated air total temperature are considered to study the combustion stabilization process. It is 1100.0 K in the first case, hereafter referred to as case RFSC-LST, and 1400.0 K in the second, hereafter referred to as case RFSC-HST. Fuel is injected sonically at room temperature. Table 1 gathers the main parameters that characterize the fuel and vitiated air inlet streams for both cases. Upstream of the left boundary of the present computational domain, the air inlet flow has been accelerated by a Mach 2.2 nozzle and passed through the isolator. With the objective of imposing vitiated air inlet temperature and velocity profiles as realistic as possible, preliminary simulations of the airflow in the isolator have been conducted for both conditions considering $\mathrm{M}_0 = 2.2$ and $T_0 = 1100$ K for case RFSC-LST, and $\mathrm{M}_0 = 2.2$ and $T_0 = 1400$ K for case RFSC-HST. The pressure at the inlet of the computational domain is determined from an isentropic evolution, with the value of the heat capacity ratio γ being set to 1.313 and 1.287 for cases RFSC-LST and RFSC-HST, respectively, thus resulting in pressure values equal to 55.410 kPa and 55.426 kPa.

The unsteady viscous flows inside the isolator have been simulated with the same LES solver (`CREAMS`). As emphasized above, the objective of these preliminary computations is only to impose realistic mean profiles for both the temperature and velocity at the inlet of the main simulations. Taking advantage of the results issued from these preliminary computations of the isolator, the filtered temperature and velocity components are settled from the computed profiles of the averaged temperature $\left\{\widetilde{T}\right\}$ and velocity components $\{\widetilde{u}_i\}$ obtained at the outlet of the isolator. However, it should be acknowledged that, in comparison with some previous studies, e.g., Kawai and Lele (2010), no special effort has been spent to represent the unsteady (i.e., turbulent) features of the supersonic boundary layer at the inlet of the main simulation. In Kawai and Lele (2010), a concurrent supersonic turbulent boundary layer (STBL) simulation has been conducted by making use of rescaling and reintroduction procedures. The inflow conditions for the main JISCF simulation were extracted from a plane of the concurrent STBL simulation. Other strategies based on the use of synthetic inlet turbulence generators could have been also retained to model the present fluctuating inflow conditions but, previous analyses, see for instance Vedovoto et al. (2015), showed that, even with properly set mean velocity and turbulence kinetic energy, the resulting flowfields still remain very sensitive to the arbitrary choice of the synthetic turbulence model. Therefore, for the purpose of the present study, which is focused on other specific issues, a simpler solution has been chosen with no fluctuations imposed at the inlet boundary.

The fuel injection boundary layer is taken into account by setting the following velocity profile $u(r,t) = f(t) \cdot [u_w - (\mathrm{U}_1 - u_w)\,\mathrm{erf}\,((r - r_1)/(2.0\,\alpha\, r_1))]$ with $\alpha = 0.05$, where U_1 denotes the hydrogen inlet bulk flow velocity, u_w is the flow velocity in the direct vicinity of the wall, r is the distance to the center of the fuel injection, and $r_1 = D_1/2.0 = 1.25$ mm is the radius of the fuel injection port. The function $f(t) = 1.0 - \exp\,(-5.0\,t/t_1)$ has been used to avoid numerical instabilities that may arise when the mass flow rate is applied directly. In this expression, $t_1 = 0.2\,\mu\mathrm{s}$ is the characteristic time required for the injection to be fully established.

Time is made non-dimensional by considering its product with the ratio of the fuel injection port diameter D_1 to the fuel inlet bulk flow velocity U_1. The simulations are started at $t^* = \mathrm{U}_1\, t/D_1 = 0.0$ without any fuel injection and are run without any chemical reaction until the fuel injection is developed in the whole computational domain. A typical snapshot depicting an iso-surface ($\widetilde{\xi} = 0.5$) of the fuel inlet tracer[1] is presented in Fig. 3. Chemical reactions are then activated at $t^* = 300.0$, i.e., after a fuel particle got enough time to cross the entire computational domain, and the simulation is run up to $t^* = 1200.0$. Datafiles are stored at a frequency 1.0 MHz. During the numerical simulations, the CFL number value has been varied between 0.3 and 0.7, while the Fourier number Fo has been set constant and equal to 0.9.

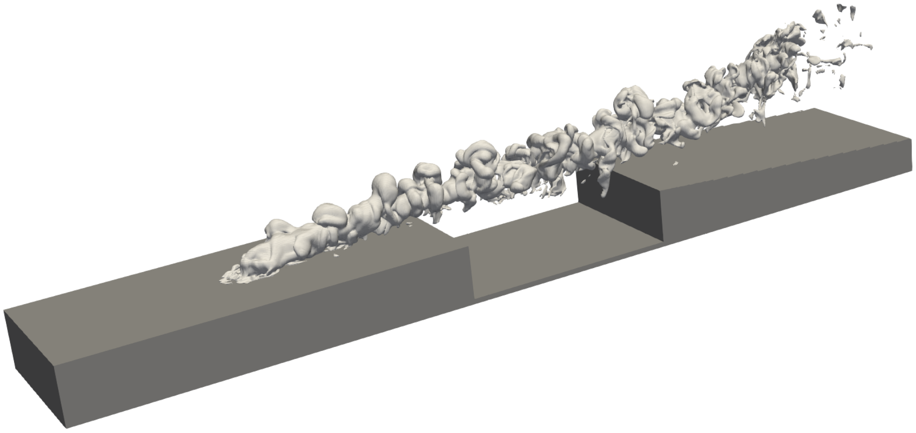

Figure 3: Iso-surface ($\widetilde{\xi} = 0.5$) of the fuel inlet tracer at time $t^* = 350.0$ (case RFSC-LST)

4. Mesh reliability analysis

The retained numerical schemes together with the choice of SGS modelling closures, see section 2, are well-known to be essential ingredients of any LES computations (Garnier et al., 2009). They do not, however, constitute the sole issues that must be properly addressed: it is indeed also worth recalling that the computational resolution is itself of the utmost importance. For instance, in wall-bounded flows such as those considered herein, the integral

---

[1] This quantity will be further discussed in the next section.

scale, away from the walls, is proportional to the turbulent boundary-layer thickness and the resolution requirement is determined by the range of scales contributing to the desired statistics. Mostly, the turbulent kinetic energy production results from high-speed streaks, which remain confined within a very small region in the direct vicinity of the wall (Kline et al., 1967). The corresponding flow structures are extremely small when compared to the overall flow dimensions. These small structures, however, play an essential role in the turbulent boundary layer dynamics and therefore need to be well resolved. The design of the computational mesh and associated levels of resolution thus result from a compromise between turbulent dynamics reproduction and CPU costs. Based on the non-reactive computed flowfields, the present section will provide a detailed mesh reliability analysis. In this respect, it must be acknowledged that obtaining a strict proof of computational resolution adequacy remains quite challenging and instead, as documented in the present section, one can gather various clues that all bring support to the mesh quality assessment analysis. The conclusion drawn from this mesh reliability analysis will be confirmed by the subsequent inspection of the computed reactive flows.

	DNS	wall-resolved LES
Δx^+	$10-15$	$50-150$
Δy^+	1	<2
Δz^+	5	$10-40$

Table 3: Recommended computational mesh size in wall units (Piomelli and Chasnov, 1996; Pope, 2000; Piomelli and Balaras, 2002)

There exist many criteria to asses the mesh resolution quality. Some of them are based on mathematical estimates, while others rely on rather heuristic arguments. For instance, Table 3 presents recommended orders of magnitude of computational mesh cell sizes for both DNS and wall-resolved LES computations. In this table, the values of Δx^+, Δy^+, and Δz^+ denote the dimensions of the computational cells present at the wall location expressed in wall units, i.e., $\Delta x^+ = \Delta x_1/l_w$, $\Delta y^+ = \Delta x_2/l_w$, and $\Delta z^+ = \Delta x_3/l_w$. We recall that the wall characteristic length scale l_w is given by $l_w = \mu_w/\sqrt{\rho_w \tau_w}$, where $\tau_w = \mu_w \left(\partial \langle u_1 \rangle / \partial x_2\right)_w$ denotes the stress at the wall with $\langle u_1 \rangle$ the statistically-averaged value of the longitudinal velocity component (Lesieur et al., 2005). It is noteworthy that this value is presently estimated from the average of the filtered velocity component.

Figure 4 reports the distributions of the dimensions of the computational cells present at the wall location, expressed in wall units. The top subfigure, i.e., Fig. 4a, corresponds to distributions obtained for case RFSC-LST, while the distributions obtained for case RFSC-HST have been gathered in the bottom subfigure, i.e., Fig. 4b. Since the focus of the present study is placed on the reactive flow development, these distributions correspond to values obtained in cells where the filtered mixture fraction $\widetilde{\xi}$ is such that $0.001 \leq \widetilde{\xi} \leq 0.999$, thus excluding non-reactive mixtures associated to pure fuel or pure oxidizer. The inspection of these distributions confirms that the wall-resolved LES criteria of Table 3 are quite satisfactorily fulfilled.

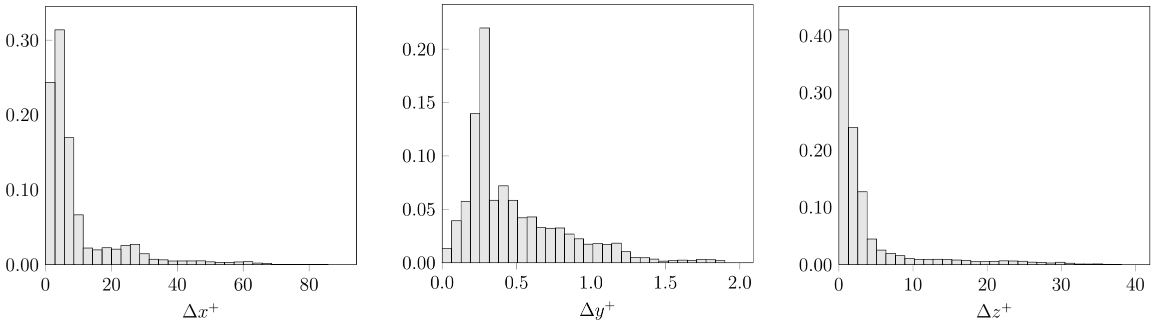

(a) case RFSC-LST

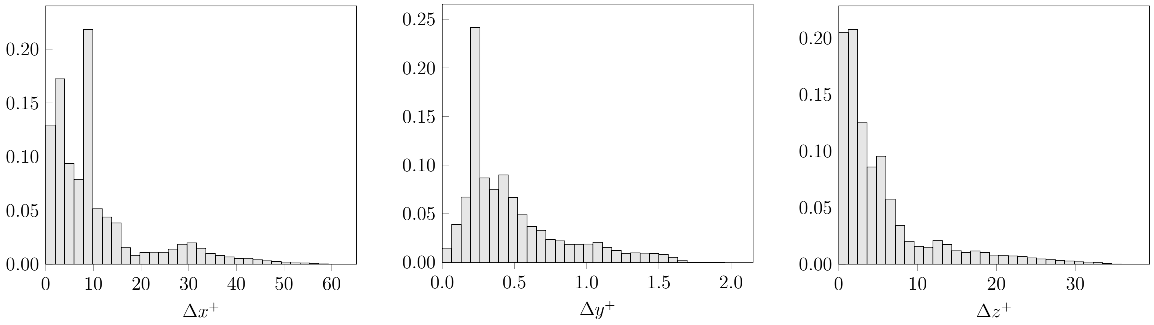

(b) case RFSC-HST

Figure 4: Normalized computational mesh size histograms

The mesh resolution quality in the vicinity of the walls is then assessed through a more detailed analysis of the averaged boundary layer flow. To this purpose, we consider again normalized quantities. In this respect, the longitudinal component of the non-dimensional mean velocity is defined by $\langle u_1 \rangle / u_{\tau_w}$ with $u_{\tau_w} = \sqrt{\tau_w / \rho_w}$ the wall friction velocity. Figure 5 displays the profiles, in wall units, of the normalized mean velocity u^+ together with the logarithm of the viscosity ratio, i.e., $\log \left(\mu_{\mathtt{SGS}} / \langle \widetilde{\mu} \rangle \right)$, plotted versus the distance to the wall at several locations x_1/D_1. Here, the mean values have been obtained from an average performed over instantaneous snapshots of the median plane (i.e., $x_3/D_1 = 0.0$). Despite the visible shift of the velocity in the logarithmic zone, these profiles confirm that the WALE model satisfactorily changes its behavior in the buffer layer that separates the logarithmic zone ($y^+ > 30.0$) from the viscous sublayer ($y^+ < 5.0$). Moreover, once plotted in logarithmic coordinates, the viscosity ratio increases almost linearly, which is consistent with its expected behavior (Nicoud and Ducros, 1999; Techer et al., 2018).

The assessment of the computational resolution is completed through a detailed mesh quality analysis. In this purpose, two quality indexes are considered. The corresponding quantities vary from zero (i.e., poor mesh resolution) to unity (i.e., good mesh resolution): the higher the value of the index, the better the resolution. First, we consider the modified quality index of Pope (2004), which is defined as follows: $\mathrm{IQ}_k = k/(k + k_{\mathtt{SGS}})$, where k denotes the resolved turbulent kinetic energy and $k_{\mathtt{SGS}}$ is its subgrid-scale unresolved counterpart, which is presently evaluated from the Yoshizawa closure $k_{\mathtt{SGS}} = \nu_{\mathtt{SGS}} / \left(\mathrm{C}_M \Delta \right)^2$ with $\mathrm{C}_M =$

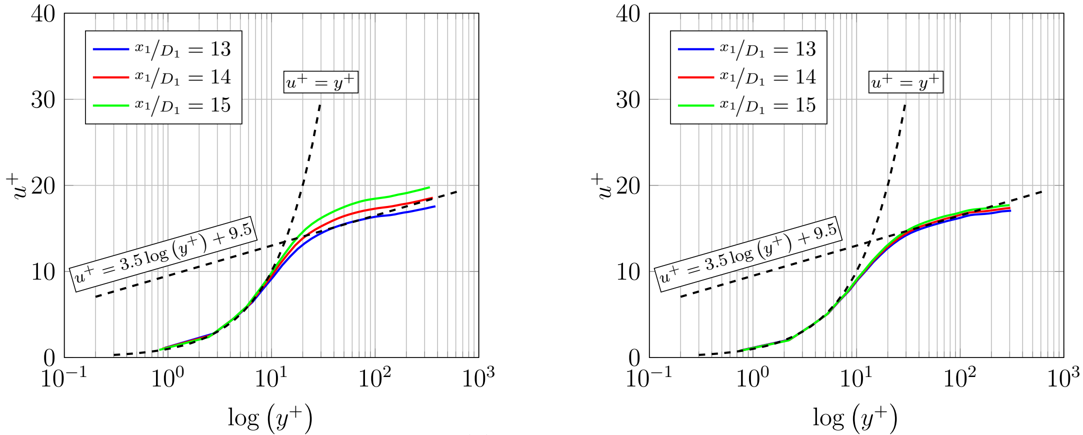

(a) Velocity

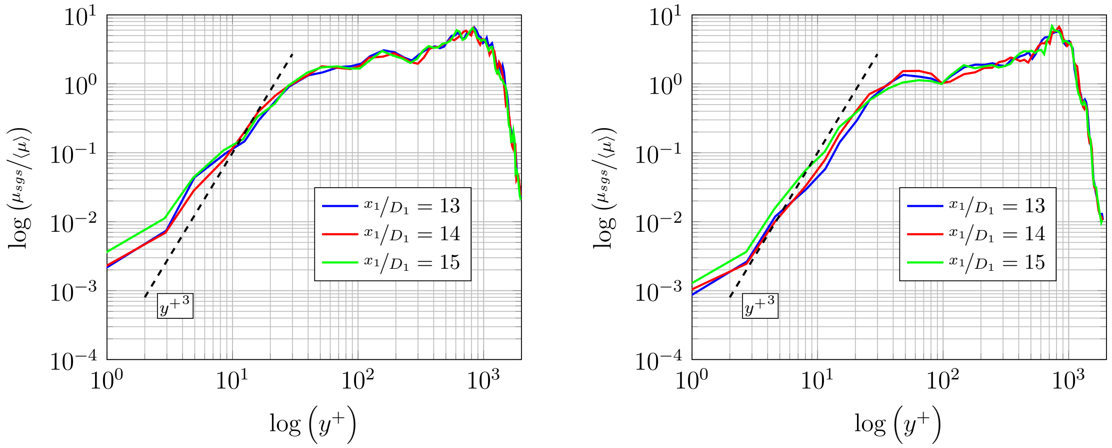

(b) Viscosity ratio

Figure 5: Non dimensional velocity profile in wall units and viscosity ratio profile at several locations x_1/D_1 for cases RFSC-LST (left) and RFSC-HST (right)

0.069 (Yoshizawa, 1986). According to Pope (2004), the mesh resolution could be considered as sufficient, provided that the value IQ_k exceeds 0.80, which means that at least eighty percent of the turbulent kinetic energy is captured at the resolved scale. However, this quality index may display some sensitivity to the SGS modelling and, therefore, it seems worthwhile to complete the analysis with other estimates. To this purpose, the quality index of Celik et al. (2005) is also considered. It is based on a comparison between the computational grid characteristic size and the Kolmogorov length scale, as given by $\mathrm{IQ}_\eta = \left(1 + \alpha_\eta(\Delta/\ell_\eta)^m\right)^{-1}$, with $(\alpha_\eta, m) = (0.05, 0.5)$ and ℓ_η evaluated from the following scaling rule $\ell_\eta = \left(\nu^3/\varepsilon\right)^{1/4}$ with ε being the turbulent kinetic energy dissipation rate. In this respect, it seems worth recalling that a standard criterion for DNS computation is $k_{max} \cdot \ell_\eta = 3/2$ in such a manner that, approximating k_{max} from π/Δ (Pope, 2000), it leads to a value of Δ/ℓ_η approximately equal to 2.0. Once introduced in the expression of the quality index IQ_η, this gives $\mathrm{IQ}_\eta = 0.93$. This means that, in regions characterized by $\mathrm{IQ}_\eta \geq 0.93$, the computational resolution can be considered as equivalent to the fulfillment of a standard DNS resolution criterion.

Figure 6 displays the probability density function (PDF) of the two quality indexes ob-

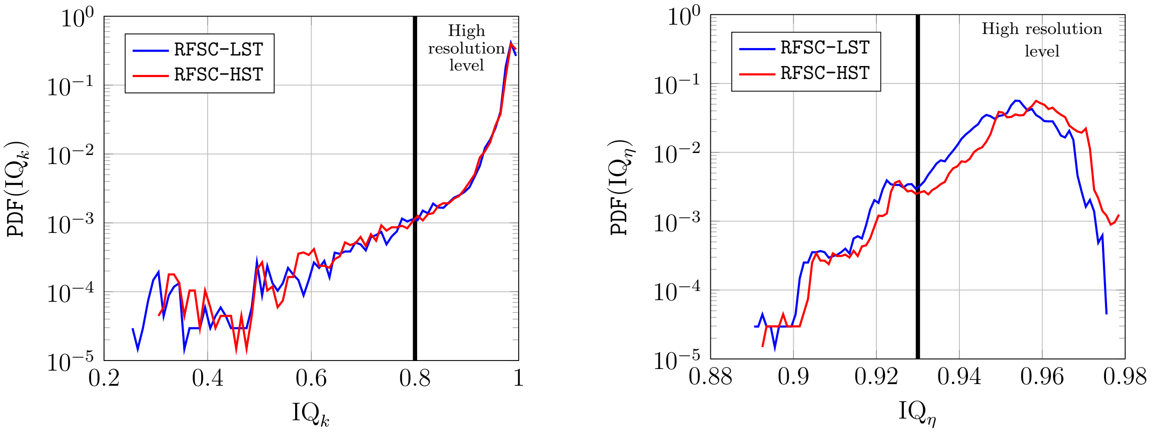

(a) IQ_k (Pope, 2004)

(b) IQ_η (Celik et al., 2005)

Figure 6: PDF of the quality index obtained in the median plane along the spanwise direction (i.e., $x_3/D_1 = 0.0$)

tained in the medium plane ($x_3/D_1 = 0.0$) of the computational mesh. The corresponding statistics show that most of the obtained values of the quality index IQ_k (resp. IQ_η) are larger than 0.80 (resp. 0.93). This conclusion can be more firmly and quantitatively assessed from a direct inspection of the cumulative distribution function (CDF), the expression of which is given by

$$\mathbb{F}(x) = \int_0^x \mathtt{PDF}(\mathrm{IQ})\, \mathrm{dIQ} \tag{11}$$

and its complement to unity

$$1 - \mathbb{F}(x) = 1 - \int_0^x \mathtt{PDF}(\mathrm{IQ})\, \mathrm{dIQ} = \int_x^1 \mathtt{PDF}(\mathrm{IQ})\, \mathrm{dIQ} \tag{12}$$

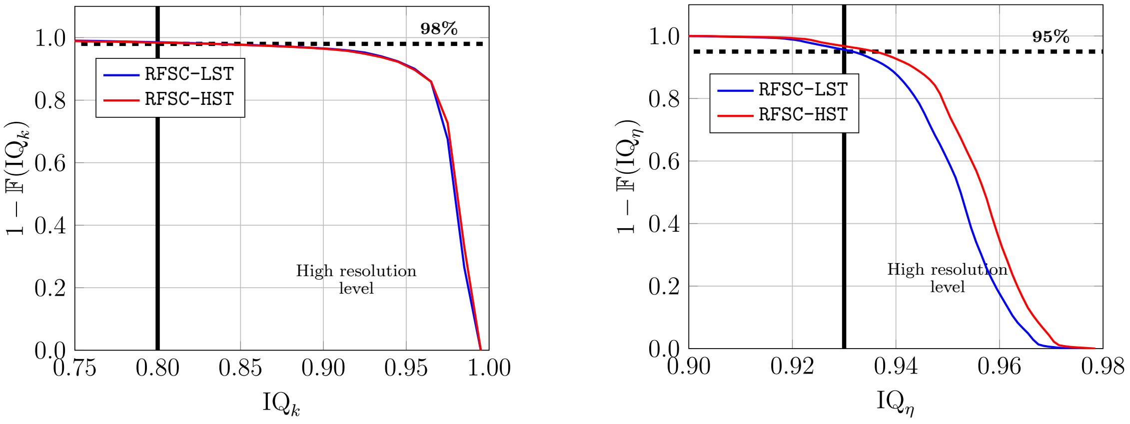

(a) IQ_k (Pope, 2000)

(b) IQ_η (Celik et al., 2005)

Figure 7: Value of $1-\mathbb{F}(\mathrm{IQ})$, i.e., value of the probability to have a quality index larger than IQ. The probability to reach a level of the quality index larger than 0.80 for IQ_k and larger than 0.93 for IQ_η are also delineated.

The second expression, i.e., the one provided by Eq. (12), measures the probability of having a value of the quality index IQ larger than x. Figure 7 thus shows that almost 98% of the values of the Pope quality index IQ_k are larger than 0.80. It also reveals that 95% of the values of the quality index IQ_η are larger than 0.93, a value that corresponds to the standard DNS resolution requirement discussed above.

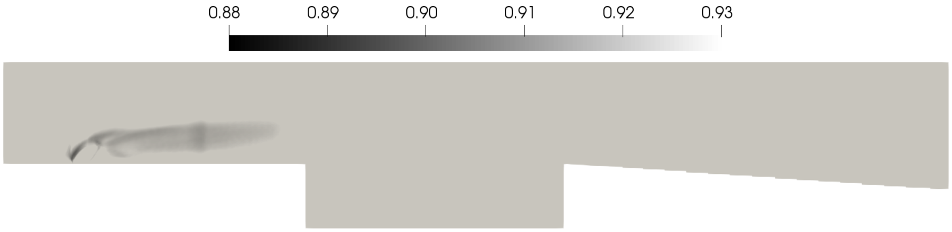

(a) case RFSC-LST

(b) case RFSC-HST

Figure 8: Mean fields of the index IQ_η obtained in the median plane along the spanwise direction ($x_3/D_1 = 0.0$)

Finally, Fig. 8 reports the mean field of IQ_η obtained in the median plane along the spanwise direction ($x_3/D_1 = 0.0$). This figure confirms that the vicinity of the fuel injection and the shear layer that develops above the wall-mounted cavity display quite satisfactory levels of resolution. The resolution level is also excellent upstream of the fuel inlet port and only slightly decreases downstream of the hydrogen injection; even in this region, the values of IQ_η indeed remain such that $\mathrm{IQ}_\eta \geq 0.90$. The inference from all the quantities discussed above is that the present set of computations indeed displays a high level of resolution. As summarized in section 2, this high level of resolution is combined with the use of high-precision numerical schemes and subgrid-scale models that satisfactorily recover the DNS limit, thus resulting in solid bases to perform high-fidelity numerical simulations.

operator	definition
$\bar{\Phi}$	(spatially-) filtered value
$\widetilde{\Phi} = \overline{\rho\Phi}/\overline{\rho}$	(spatially-) Favre-filtered value
$\langle\Phi\rangle$	(temporal-) averaged value
$\{\Phi\} = \langle\rho\Phi\rangle \,/\, \langle\rho\rangle$	(temporal-) Favre-averaged value

Table 4: Expressions of spatial filtering and temporal averaging operators

Finally, it must be underlined that the targeted objective is the simulation of the reactive flow stabilization and we are not really interested by the description of the flow inside the exit nozzle. Therefore, the mesh has been considerably coarsened in this region of the computational domain and no special effort has been spent to describe the flow in this part of the combustor. As a consequence, there are some pressure disturbances that appear at the nozzle wall at the level of each cell transition. The birth of such perturbations in the exit nozzle is visible on numerical schlieren images and has been already reported in the literature when coarse meshes are considered.

5. Analysis of computational results

5.1. Statistical convergence of the computational datasets

Before proceeding with a detailed inspection of the computational results, we proceed with a statistical convergence analysis. Therefore, in an attempt to verify the convergence of the second-order moments of the velocity field, eight probes are placed in the median plane of the computational domain (i.e., $x_3/D_1 = 0.0$), as depicted in Fig. 9. Table 4 summarizes the various spatial filtering and temporal averaging operators. At this level, it should be emphasized that, for the present application to LES data, the temporal operator is applied to filtered quantities. For instance, the temporal average of the density is evaluated from the resolved density field using $\langle \overline{\rho} \rangle$.

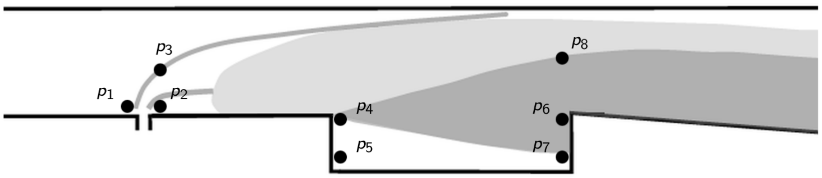

Figure 9: Probes location for the second-order moments convergence verification

Recalling that the second-order centered moment of any quantity Φ is the expected value of the squared deviation from its mean, i.e., $\sigma_\Phi^2 = \left\langle \left(\Phi - \langle \Phi \rangle\right)^2 \right\rangle = \left\langle \Phi^2 \right\rangle - \langle \Phi \rangle^2$, the temporal convergence of the second-order moments of the filtered velocity field $\widetilde{u}_i$ is checked by evaluating the following expression:

$$\mathrm{R}_{\widetilde{u}_i} = \langle \widetilde{u}_i \widetilde{u}_i \rangle - \langle \widetilde{u}_i \rangle \langle \widetilde{u}_i \rangle - \left\langle \left(\widetilde{u}_i - \langle \widetilde{u}_i \rangle\right)^2 \right\rangle \tag{13}$$

The above quantity, i.e., the residual $\mathrm{R}_{\widetilde{u}_i}$, should be zero provided that $\left\langle \langle \widetilde{u}_i \rangle \langle \widetilde{u}_i \rangle \right\rangle = \langle \widetilde{u}_i \rangle \langle \widetilde{u}_i \rangle$ and $\left\langle \langle \widetilde{u}_i \rangle \widetilde{u}_i \right\rangle = \langle \widetilde{u}_i \rangle \langle \widetilde{u}_i \rangle$, which provides an excellent verification of the convergence of the temporal averaging operator.

Figure 10 displays the statistical convergence of the longitudinal and transverse components of the velocity field for cases RFSC-LST and RFSC-HST as obtained on the various probes defined in Fig. 9. From these results, one can notice that the solution convergence is obtained for $t^* \geq 800.0$ and $t^* \geq 900.0$ for cases RFSC-LST and RFSC-HST, respectively. Therefore, the statistical post-processing of the computational results will be performed over snapshots obtained from these values up to the end of the simulation.

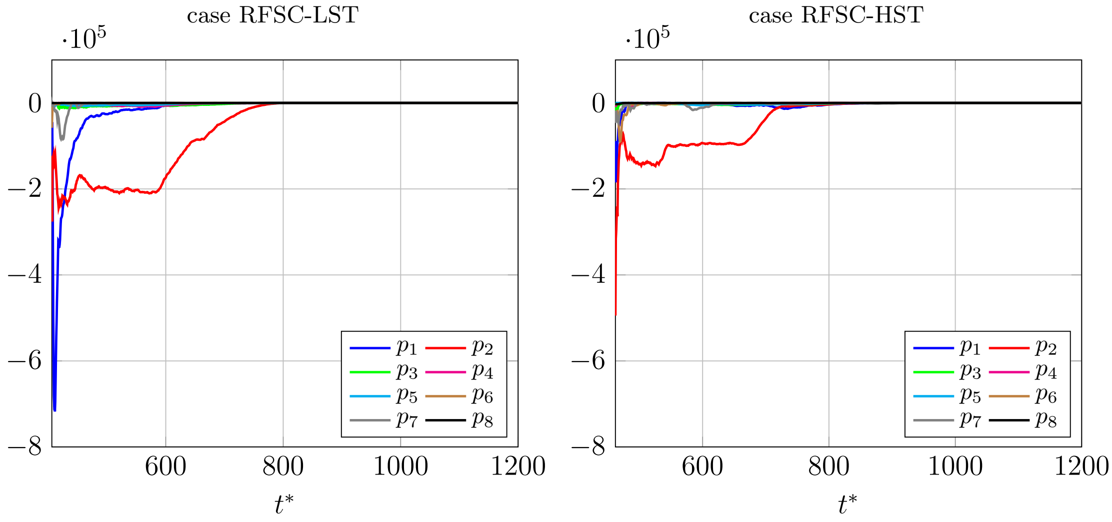

(a) Second-order residual of the longitudinal filtered velocity component $\mathrm{R}_{\widetilde{u}_1}$

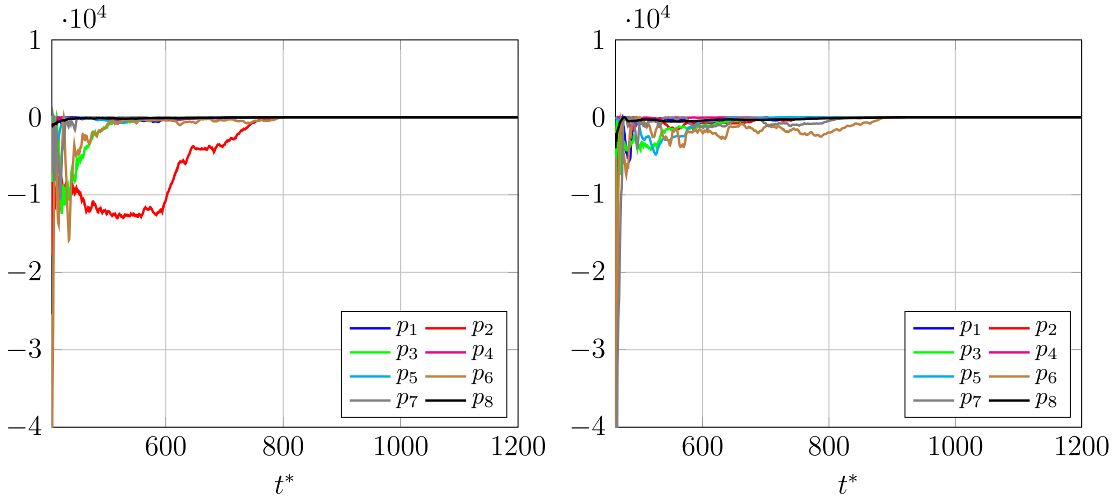

(b) Second-order residual of the transverse filtered velocity component $\mathrm{R}_{\widetilde{u}_2}$

Figure 10: Convergence of the second-order moments of filtered velocity at the probe locations defined in Fig. 9

5.2. Non-reactive flow analysis

Figure 11 displays an instantaneous numerical Schlieren image in the median plane together with an iso-surface of the fuel mass fraction ($\widetilde{Y}_{\mathrm{H}_2} = 0.5$) colored by the normalized filtered temperature field $\widetilde{T}/T_0$ for cases RFSC-LST and RFSC-HST. The topology of JISCF compressible flowfield has been largely discussed in the literature for both non-reactive (Kawai and Lele, 2010) and reactive conditions (Ben Yakar and Hanson, 1998). The hydrogen underexpanded jet quickly expands through a Prandtl-Meyer fan at the boundary of the jet orifice prior to being compressed through a barrel shock and a Mach disk. The jet forms two series of counter-rotating vortices the rotation axis of which are aligned with the downstream direction. At the fuel injection location, the supersonic vitiated airstream is blocked by the

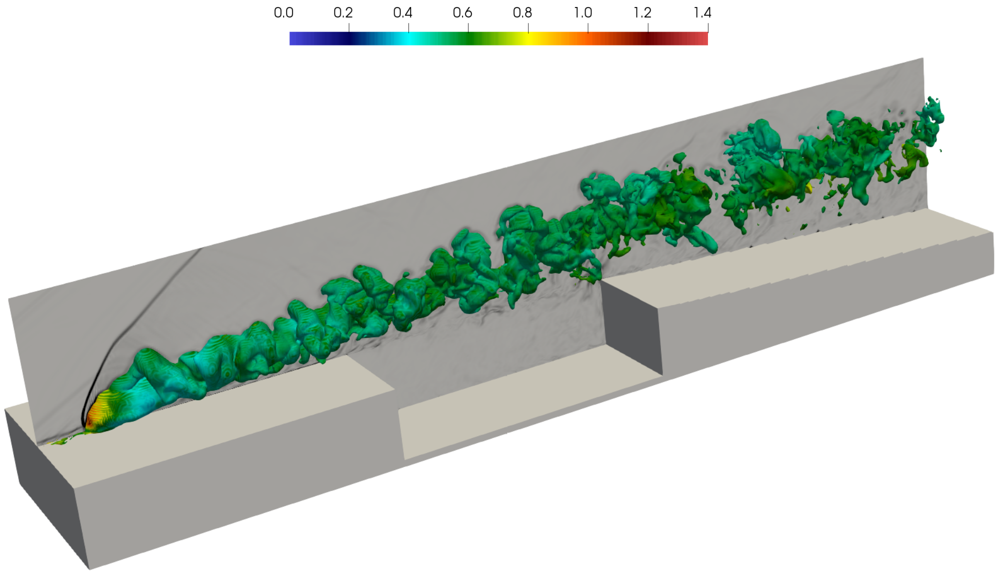

(a) case RFSC-LST

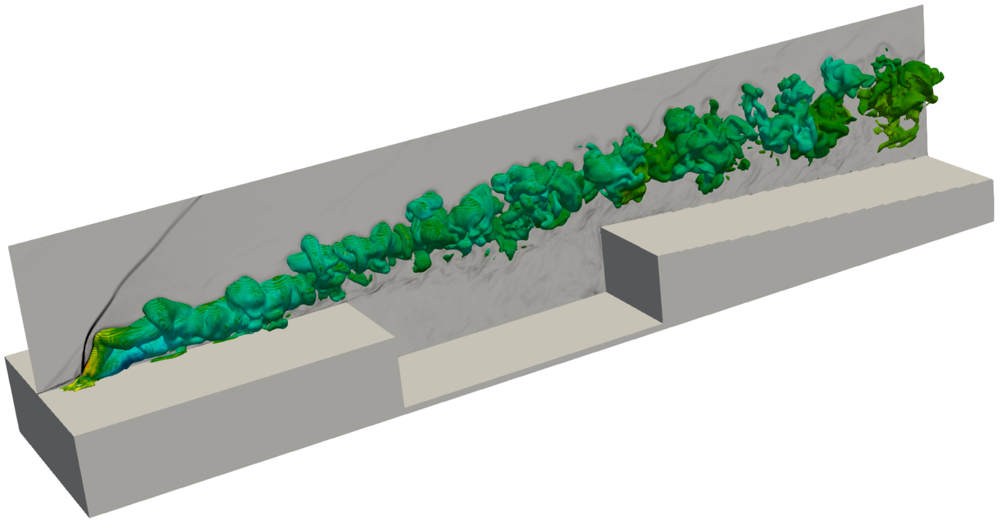

(b) case RFSC-HST

Figure 11: Instantaneous numerical Schlieren in the median plane together with an iso-surface of the fuel mass fraction colored by the normalized temperature field

highly underexpanded[2] transverse jet of hydrogen, with compression waves leading to the birth of a three-dimensional bow shock created ahead of the jet. It causes boundary layer separation and leads to the formation of a horseshoe vortex region downstream of the jet. The mixing process mainly takes place downstream of the barrel shock because there is a very high velocity gradient between the hydrogen jet and the crossflow. This triggers the birth of large-scale coherent structures induced by the Kelvin-Helmholtz (K-H) instabilities. Further downstream, the scale reduction processes come into play, thus leading to the breakup of these

---

[2] The nozzle pressure ratio (NPR) is larger than ten.

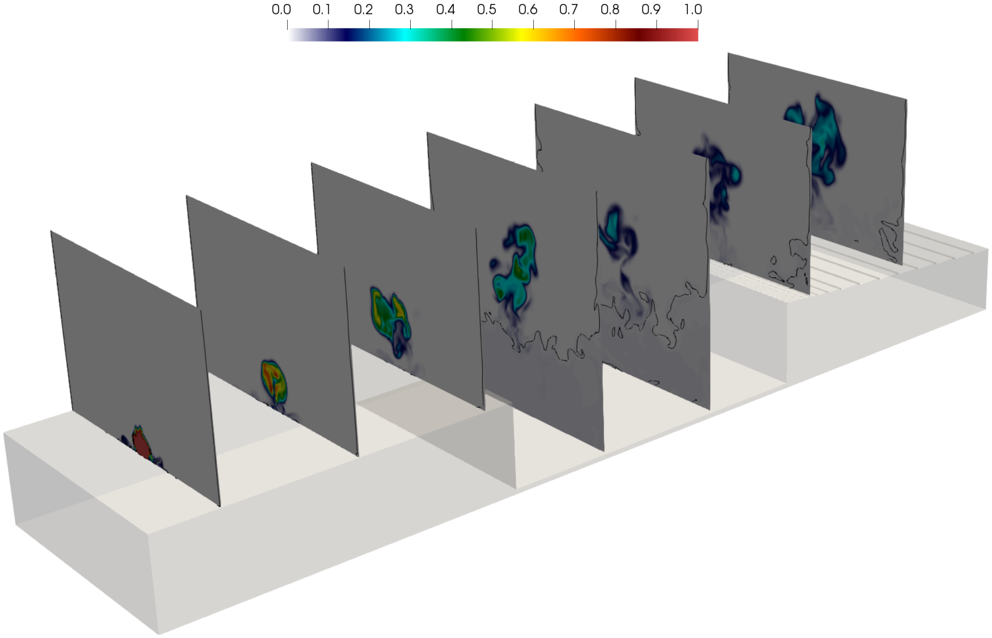

(a) case RFSC-LST

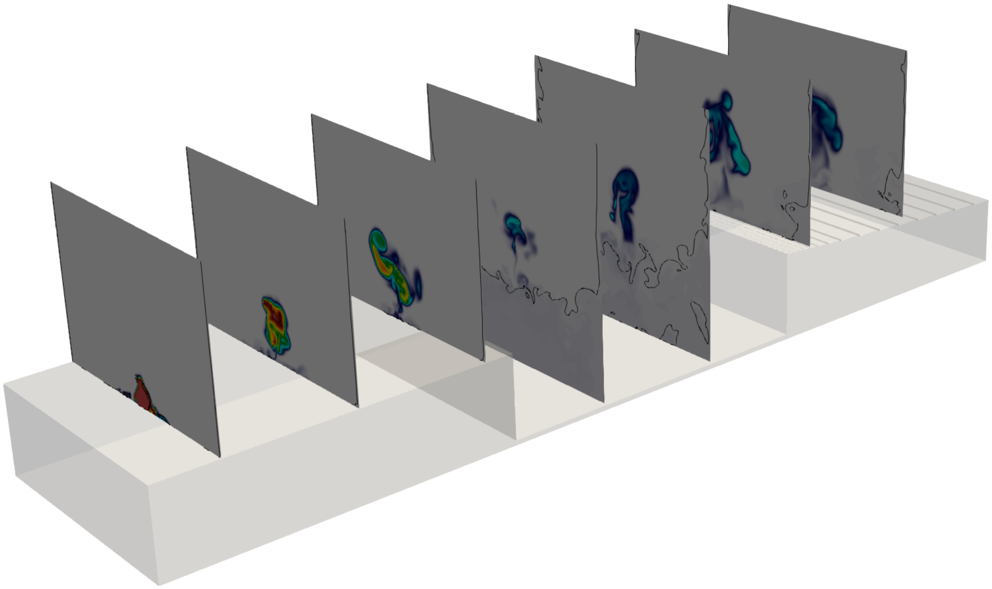

(b) case RFSC-HST

Figure 12: Instantaneous contours of fuel mass fraction together with the sonic iso-line (in black) in several spanwise planes

large-scale vortices.

Figure 12 reports instantaneous contours of fuel jet mass fractions together with the sonic iso-line in several spanwise planes. The mixing between fuel and oxidizer starts at the fuel jet injection with most of the fuel spread into the supersonic flow. The fuel jet is however slightly torn up by the cavity low-speed flow, with a small part of the hydrogen flowing into the wall-mounted cavity, which should result in some mixing enhancement due to recirculation zones present in the cavity. This may be checked through a mixing efficiency analysis.

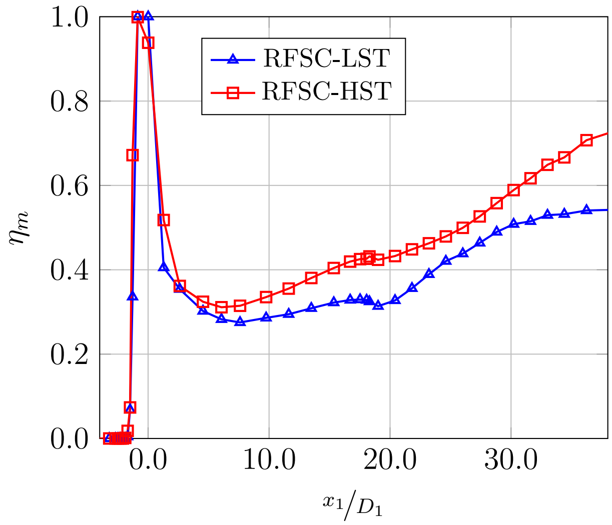

Figure 13: Mixing efficiency profile along the streamwise direction. The wall-mounted cavity extends from $x_1/D_1 = 17.8$ to $x_1/D_1 = 38.1$.

The corresponding fuel mixing degree is indeed a critical parameter to evaluate the supersonic combustor performance as a whole. In this respect, there exist many possible definitions of the mixing efficiency in the literature, see for instance Moule et al. (2014b) and Liu et al. (2017). This quantity, i.e., the fuel mixing degree, can be defined as the mass flow rate ratio of reactants that would react to the total mass flow rate of reactants (Liu et al., 2017):

$$\eta_m(x_1) = \int_{\mathcal{A}(x_1)} \overline{\rho}\, \widetilde{u}_1\, Y_{\mathrm{H}_2,r}\, \mathrm{d}A \Big/ \int_{\mathcal{A}(x_1)} \overline{\rho}\, \widetilde{u}_1\, \widetilde{Y}_{\mathrm{H}_2}\, \mathrm{d}A \tag{14}$$

where, following Liu et al. (2017), the mass fraction of reactants that would be involved in the reaction $Y_{\mathrm{H}_2,r}$ is evaluated by assuming a complete oxidation of the available amount of hydrogen:

$$Y_{\mathrm{H}_2,r} = \begin{cases} \widetilde{Y}_{\mathrm{H}_2} & \widetilde{Y}_{\mathrm{H}_2} \leq Y_{\mathrm{H}_2,st} \\ Y_{\mathrm{H}_2,st}(1-\widetilde{Y}_{\mathrm{H}_2})/(1-Y_{\mathrm{H}_2,st}) & \widetilde{Y}_{\mathrm{H}_2} \geq Y_{\mathrm{H}_2,st} \end{cases} \tag{15}$$

with $Y_{\mathrm{H}_2,st}$ the fuel mass fraction at stoichiometry. In Eq. (14), the elementary transverse surface element $\mathrm{d}A$ is evaluated from the product $\Delta x_2 \cdot \Delta x_3$ and, at each location x_1, the integral is performed over the whole transverse section $\mathcal{A}(x_1)$.

Figure 13 displays the mixing efficiency profile obtained along the streamwise direction, zooming at the fuel injection and wall-mounted cavity, i.e., in a region delineated by $-4.0 \leq x_1/D_1 \leq 38.0$. The obtained results display some similarities with those previously reported by Liu et al. (2017) who retained the same definition of the mixing efficiency. Thus, the mixing efficiency is found to be close to 100% in the direct vicinity of the fuel injection, where only a small amount of fuel diffused along the turbulent boundary layer. A minimum is reached ahead of the fuel jet injection because the mixing is dominated by the large scale vortices in the jet shear layer. Then, the mixing efficiency increases faster along the cavity, which means that mixing processes are enhanced, reaching finally almost 100% at the end of the cavity.

The present set of non-reactive results is now used to perform an analysis of ignition probabilities. Mixtures of fuel and oxidizer are indeed considered to be flammable only if a premixed flame is able to propagate into the corresponding fresh reactants, which happens only within given composition limits. The flammability limits of a reactive mixture determine the lower and upper fuel concentration so that combustion can proceed. These values are obtained from well-defined experimental procedures by varying the mixture composition and they may be altered not only by temperature and pressure but also by flame propagation direction under a gravitational field (Zabetakis, 1965). The lowest fuel concentration that may lead to flame propagation is hereafter denoted as the lower flammability limit (LFL), while the largest fuel concentration is called the upper flammability limit (UFL). Both LFL and UFL are expressed in terms of volume percentages in normal conditions, i.e., at 298 K and 1.0 atm. For instance, the LFL and UFL values for mixtures of hydrogen with air are 4% and 75% (Zabetakis, 1965), which correspond to mixture fraction values equal to 0.003 and 0.167, respectively. At this level, it should be emphasized that there exist several possible ways to evaluate the mixture fraction. Discarding Lewis number effects, i.e., assuming the mixture fraction molecular diffusion coefficient equal to thermal diffusivity, this quantity may be thought as a fuel inlet tracer (Gomet et al., 2015), the value $\widetilde{\xi}_f$ of which can be evaluated from a filtered passive scalar transport equation with boundary conditions set to zero ($\widetilde{\xi}_f = 0.0$) at the oxidizer inlet and unity ($\widetilde{\xi}_f = 1.0$) at the fuel inlet. The mixture fraction can also be deduced from atoms conservation. For instance, the nitrogen mass fraction $\widetilde{Y}_{\mathrm{N}_2}$, which has been considered as a non-reactive scalar in the present set of computations[3], can be used to this purpose: $\widetilde{\xi}_{\mathrm{N}_2} = 1.0 - (\widetilde{Y}_{\mathrm{N}_2}/Y^{\max}_{\mathrm{N}_2})$ with $Y^{\max}_{\mathrm{N}_2}$ the nitrogen concentration in the vitiated airstream inlet. Finally, it is also possible to evaluate the mixture fraction on the basis of the chemical reaction stoichiometry (Peters, 2000):

$$\widetilde{\xi} = \frac{\phi\left(\widetilde{Y}_{\mathrm{H}_2}/Y^{\infty}_{\mathrm{H}_2}\right) - \left(\widetilde{Y}_{\mathrm{O}_2}/Y^{\infty}_{\mathrm{O}_2}\right) + 1}{1+\phi} \tag{16}$$

where $Y^{\infty}_{\mathrm{H}_2}$ is the hydrogen mass fraction issued from the fuel inlet (unity in the present case of pure fuel injection), $Y^{\infty}_{\mathrm{O}_2}$ is the oxygen mass fraction in the vitiated airstream, and $\phi = r_{st}\left(Y^{\infty}_{\mathrm{H}_2}/Y^{\infty}_{\mathrm{O}_2}\right)$ denotes the equivalence ratio with r_{st} the stoichiometric mass ratio. These various definitions are compared in Fig. 14, which reports the averaged profiles based on the use of each definition. For the present conditions, the obtained differences appear to be so slight that they can be neglected.

From the resolved mixture fraction PDF, the ignition probability P_{ign} may be evaluated as follows:

$$\mathrm{P}_{ign} = \int_{0.003}^{0.167} \left\langle P\left(\widetilde{\xi}\right)\right\rangle \mathrm{d}\widetilde{\xi} \tag{17}$$

The field of the corresponding ignition probability P_{ign}, obtained from the averaging of data obtained in the median plane ($x_3/D_1 = 0.0$), is reported in Fig. 15 for cases RFSC-LST

---

[3] It is indeed worth noting that nitrogen is not involved in the detailed chemistry description considered in the present study.

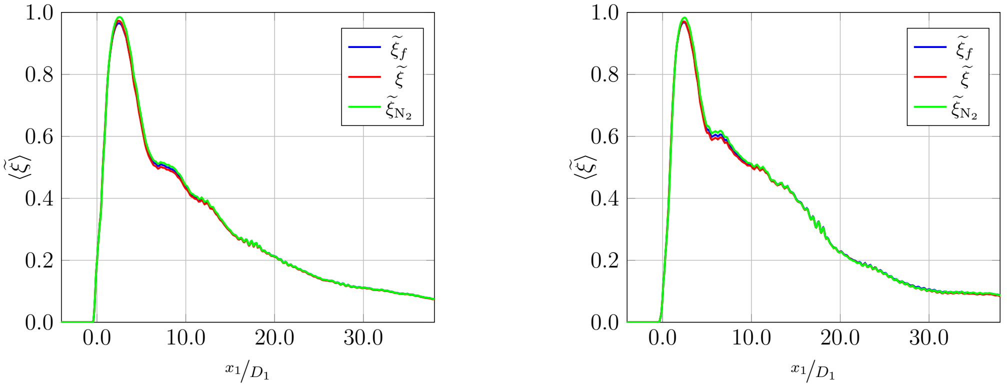

(a) case RFSC-LST

(b) case RFSC-HST

Figure 14: Averaged mixture fraction profiles obtained using three distinct definitions

and RFSC-HST. This view is restricted to a zoom for a close-up of the fuel injection and cavity regions. One can verify that, even with the present set of values of the flammability limits, which are associated to normal conditions (i.e., moderate temperature levels in the fresh reactants), the highest levels of the ignition probability P_{ign} follow quite closely the jet wake and the shear layer that develops above the cavity. It is interesting to notice that, in case RFSC-HST, there is a larger region featuring high values of P_{ign} in the vicinity of the wall downstream of the hydrogen injection. As it will be shown later on, these locations correspond to those where the jet-wake and cavity stabilization modes develop. However, it should be fairly acknowledged that the consideration of the operating temperature level of the vitiated airstream T_0, instead of the temperature 298 K associated to normal conditions, may significantly alter the results and more insights should be gained from the reactive flow simulations presented in the next section.

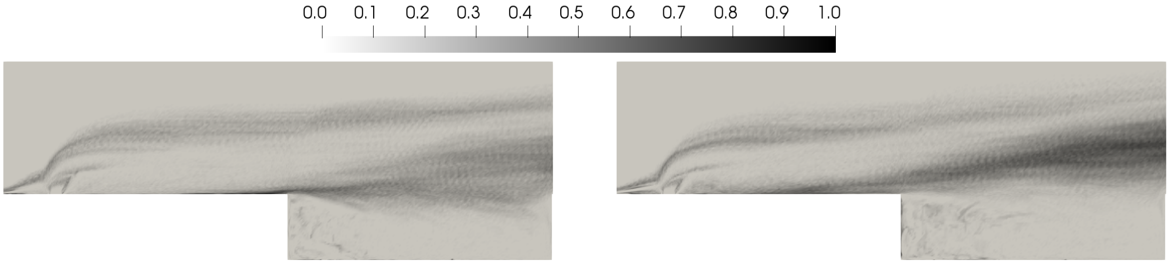

(a) case RFSC-LST

(b) case RFSC-HST

Figure 15: Ignition probability P_{ign} in the median plane $x_3/D_1 = 0.0$

5.3. Reactive flow analysis

According to the studies of Micka and Driscoll (2008), for the range of conditions reported in Micka's Thesis manuscript (Micka, 2010), the vitiated air-stream temperature T_0 plays an important role in determining the combustion stabilization mode. For inlet temperature such that $T_0 > 1350$ K, combustion stabilization occurs through a jet-wake mode, whereas for $T_0 < 1150$ K, a cavity-stabilized regime is expected. In the intermediate range ($1150 \text{ K} < T_0 < 1350$ K) combustion oscillates between the two stabilization regimes. Equation (18) may be used to approximate the fraction of time f the combustion takes place in jet-wake stabilized mode (Micka and Driscoll, 2008):

$$f = \frac{1}{2} + \frac{|T_0 - 1250.0|}{2} \operatorname{erf}\left(\frac{T_0 - 1250.0}{75.0}\right) \tag{18}$$

where the value of the vitiated airstream temperature T_0 must be provided in Kelvin S.I. unit. The corresponding function is displayed in Fig. 16 together with the two conditions studied in the present work.

From a practical viewpoint, the flame will remain in the cavity-stabilized mode for moderate values of the temperature T_0 except if a large enough fluctuation flashes it forward to a relatively stable location in the jet-wake stabilization region. If this occurs, the flame will then remain in the jet-wake stabilized mode until it becomes unstable due to another fluctuation, forcing it to flash back to a cavity-stabilized regime. The magnitude of the fluctuations required for the flame to flash back and forth becomes smaller as the temperature T_0 rises. Moreover, as T_0 is increased, the magnitude of the fluctuations that may cause the flame to flash back increases also. Thus, with the rise of the temperature T_0, combustion spends more time in the jet-wake stabilized mode, until it reaches a sufficiently high level of temperature where it cannot be destabilized by any fluctuation.

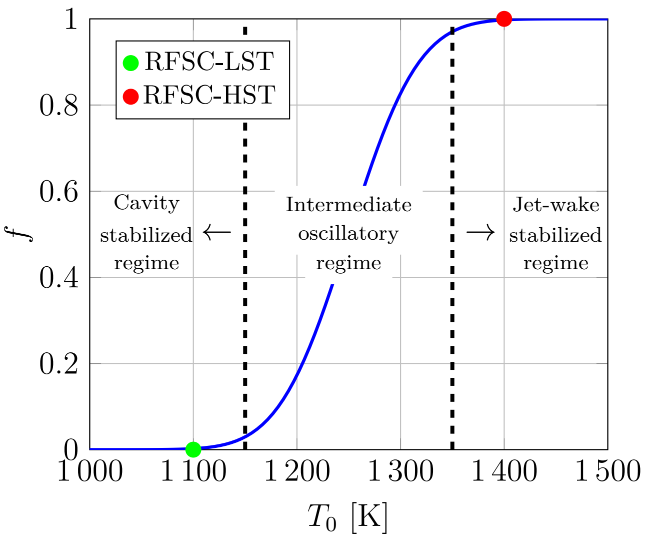

Figure 16: Combustion stabilization mode versus vitiated air-stream temperature

In the experiments, for obvious safety reasons, it is necessary to ensure that the ignition of the mixture will be successful and a spark plug located in the center of the cavity bottom wall is used. In the computations, ignition is simply obtained from the temperature increase on the rear wall of the cavity. As far as the use of adiabatic wall condition is concerned, it seems worth to emphasize that, according to the information provided by Micka (2010), after the end of the main fuel injection (end of a given run), all flow streams except the main airstream were terminated and the electric heater was turned off. The main cold stream of air continued to flow through the combustor between two consecutive runs to provide cooling before the next test. According to Micka (2010), eight combustion tests can be performed in a day. In this manner, the possible influence of experimental condition variations between the runs remains limited. Finally, it is noteworthy that the same adiabatic condition has been retained in the other (seldom) computational studies of this experimental setup, see for instance Zettervall and Fureby (2018).

In a first step of the reactive flow analysis, a comparison is performed between computational results obtained using either the PSR or the U-PaSR subgrid-scale combustion models. Such a comparison may be useful to further assess the level of computational resolution. The PSR model corresponds to the quasi-laminar approximation and consists in neglecting the possible influence of subgrid-scale fluctuations at the resolved level: the filtered reaction rates are evaluated directly from the detailed chemical scheme applied to the filtered composition. The PSR, i.e., well-stirred reactor (WSR), and PaSR representations are standardly retained as elementary building blocks of supersonic combustion modelling (Gomet et al., 2012; Potturi and Edwards, 2015; Fulton et al., 2016; Candler et al., 2017). In the present study, the U-PaSR modelling framework has been also considered (Moule et al., 2014a). Like the eddy-dissipation concept (EDC) model (Ertesvag and Magnussen, 2000), the U-PaSR is a multiscale-based model that takes into account the inhomogeneities of the composition vector $\psi = \left[T, Y_\beta\right]$ (i.e., temperature and species mass fractions) in the flame region, considering the effects of micro-mixing, finite-rate chemistry, and the interactions between them. Non-premixed combustion is assumed to take place in small dissipative structures (i.e., worms) where molecular mixing processes, which are a prerequisite before chemical reactions occur, are the most intense. It can be shown that the filtered chemical reaction rate can be expressed as follows: $\overline{\Omega}_\alpha = \overline{\rho}\,\widetilde{\omega}_\alpha = \gamma^* \overline{\Omega}_\alpha(\psi^*)$, where $\psi^* = \left[T^*, Y^*_\beta\right]$ denotes the composition of the highly dissipative fine-scale structures and γ^* measures their volume fraction. It can be shown that the U-PaSR closure recovers the DNS limit as the filter size Δ tends to zero (Moule et al., 2014a). Indeed, as $\Delta \rightarrow \epsilon$, with ϵ any arbitrary small number, we have $\gamma^* \rightarrow 1.0$ and $\psi^* \rightarrow \overline{\psi} = \psi$ and, as a result, $\overline{\Omega}_\alpha = \Omega_\alpha(T, Y_\beta)$. The SGS combustion model degenerates to its DNS counterpart, i.e., the instantaneous Arrhenius laws that are involved in the detailed chemical scheme.

Figures 17 and 18 report, respectively, the averaged cross stream profiles of OH and HO_2 mass fractions obtained at several locations x_1/D_1, considering the PSR (blue line) and the U-PaSR (red line) SGS model, for cases RFSC-LST (continuous line) and RFSC-HST (dashed line). From this figure, it is clear that the PSR and U-PaSR models lead to quite similar results. This is an outcome of the well-resolved computational meshes, which lead the subgrid-scale U-PaSR model to behave like a perfectly-stirred reactor (PSR). In the regions where chemical reactions take place, the field of γ^* — not reported for the sake of conciseness — is indeed found to approach unity and it remains larger than 0.85 as a whole. The PSR or

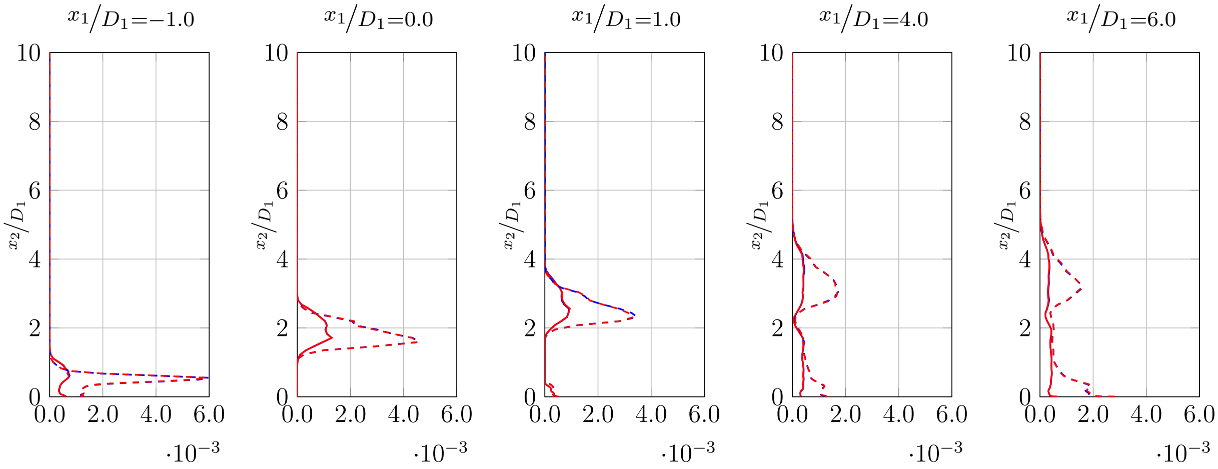

Figure 17: PSR (blue) and U-PaSR (red) OH averaged mass fraction profile comparison, for cases RFSC-LST (continuous line) and RFSC-HST (dashed line)

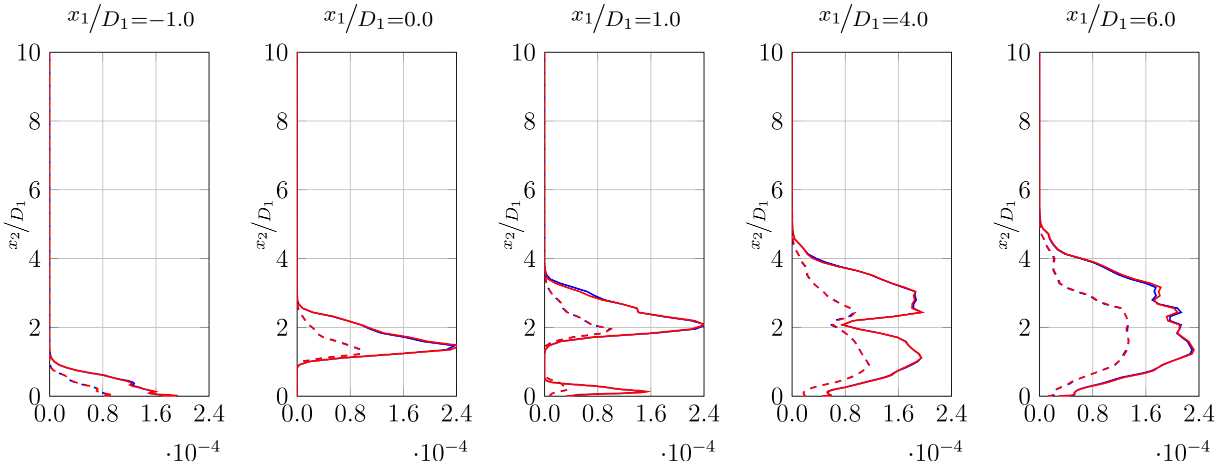

Figure 18: PSR (blue) and U-PaSR (red) HO_2 averaged mass fraction profile comparison, for cases RFSC-LST (continuous line) and RFSC-HST (dashed line)

quasi-laminar approximation thus appears as a relevant representation of chemical reactions in the present conditions, and the next steps of the discussion will therefore be restricted to computational results obtained with the PSR model.

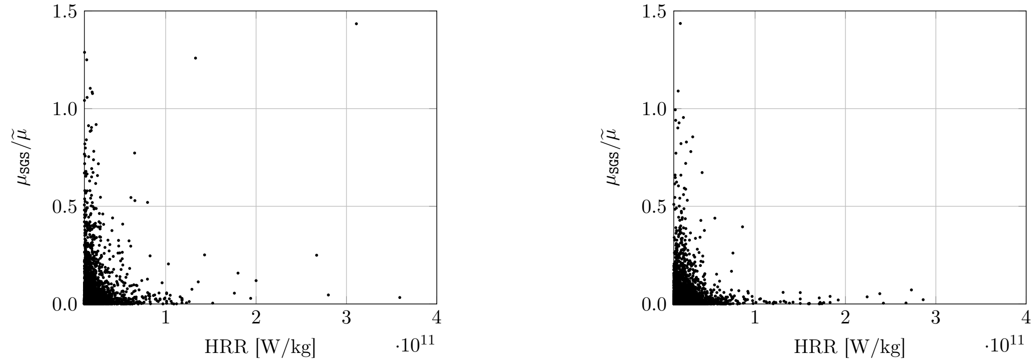

(a) case RFSC-LST

(b) case RFSC-HST

Figure 19: Scatter plot of $\mu_{\mathsf{SGS}}/\widetilde{\mu}$ versus heat release rate for (a) case RFSC-LST and (b) case RFSC-HST

At this level, it is noteworthy that the two figures discussed above, i.e., Figs. 17 and 18, reflects the quality of the computational resolution with respect to chemical processes relevant to auto-ignition and flame propagation. This is confirmed by Figs. 19 which reports the viscosity ratio $\mu_{\mathsf{SGS}}/\widetilde{\mu}$ plotted versus the heat release rate (HRR). Figure 19 clearly shows that the most important part of the HRR takes place in well-resolved regions that correspond to values of $\mu_{\mathsf{SGS}}/\widetilde{\mu}$ smaller than 0.5. In these two scatterplots, more than 99% of the points are indeed associated to values of $\mu_{\mathsf{SGS}}/\widetilde{\mu}$ smaller than 0.5. Added to Figs. 17 and 18, and to the previous inspection of resolution criteria reported in section 4, it brings some additional support in favor of computational mesh adequacy so as to capture the dynamics of the turbulent flame.

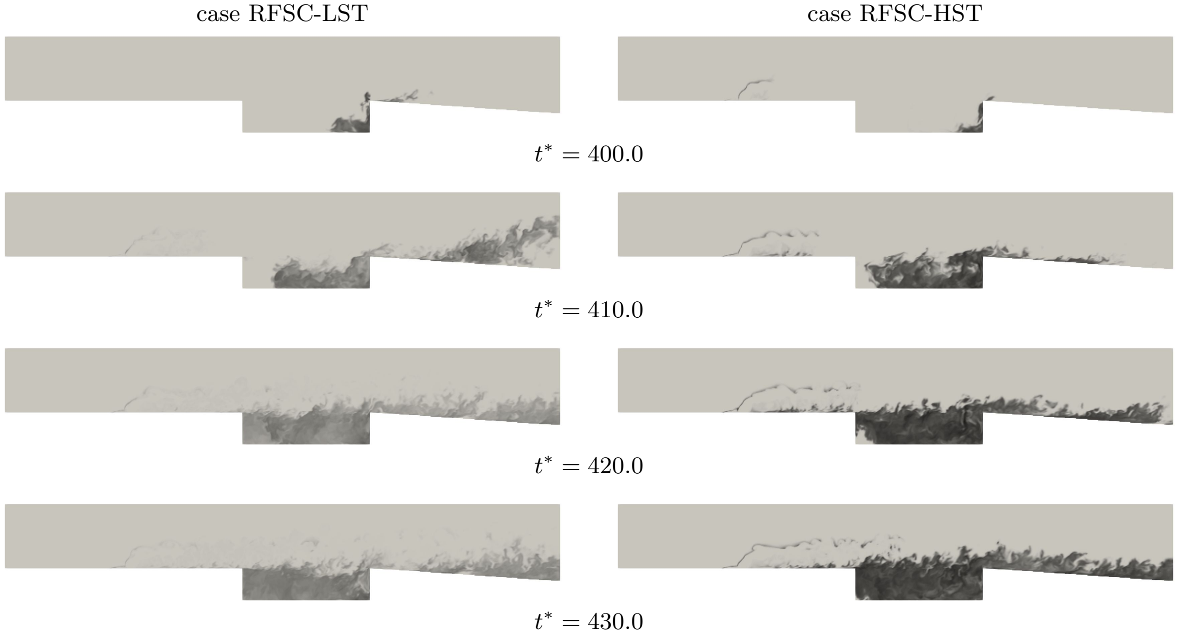

Figure 20: Temporal evolution of OH mass fraction for case RFSC-LST (left) and case RFSC-HST (right) in the median plane $x_3/D_1 = 0.0$

Figure 20 displays the temporal evolution of the OH mass fraction production rate in the median plane ($x_3/D_1 = 0.0$) for cases RFSC-LST and RFSC-HST. Chemical reactions start at the bottom end of the cavity for case RFSC-LST: it first develops within the cavity, increasing the temperature and inducing a deflection of the shear layer due to the thermal expansion induced by the heat release. The conditions then become more favorable to the spreading of chemical reactions as the combustion process develops, thus increasing the temperature and allowing the reaction zone to extend over the whole cavity, up to a point where the heat release rate becomes sufficient to stabilize the combustion process. Depending on the operating conditions, the combustion can spread upstream of the cavity, as it can be seen in case RFSC-HST. It is noteworthy that, as expected, the vitiated air-stream temperature significantly influences the combustion development. The combustion spreads significantly faster at a higher temperature. Significant H_2O production takes place along the upper part of the cavity for case RFSC-LST (cavity stabilized mode), whereas for case RFSC-HST (jet-wake stabilized mode) combustion spreads downstream of the fuel injection and within the cavity.

Figure 21 reports the averaged heat release rate issued from the computations, presented in a way similar to the flame luminosity images of Micka and Driscoll (2008). To favor the comparison with the images reported in the experimental work, the HRR has been integrated along the spanwise direction. The computational results confirm that the cavity-stabilized combustion mode is characterized by a reaction zone anchored at the leading edge of the cavity, spreading into the main flow at an approximately constant angle. In the jet-wake stabilized mode the reaction zone is stabilized upstream of the cavity and the corresponding leading edge is curved. This is fully consistent with the experimental observations. Nevertheless, it should be emphasized that such a comparison remains purely qualitative since the relation that may exist between flame luminosity and HRR remains by far unknown. It is however quite interesting to see that the global change of behaviour that is observed between case RFSC-LST and case RFSC-HST is captured by the present set of computations. As underlined at the end of section 4, the mesh has been considerably coarsened downstream of the wall-mounted cavity and there are some pressure disturbances that appear at the nozzle wall. Their imprint is clearly visible on the right side of the HRR fields reported in Fig. 21.

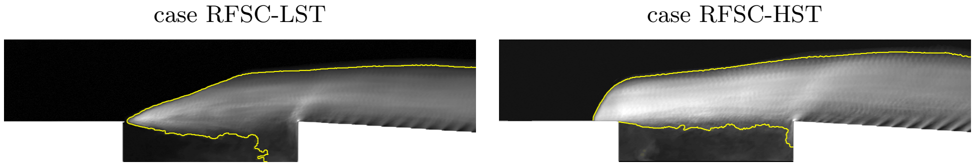

Figure 21: Averaged heat release rate (HRR) issued from the computations (arbitrary scaled units)

Thus, two distinct combustion stabilization modes can be inferred from the analysis of the reactive flowfield. Under moderate values of the airstream temperature (case RFSC-LST) the cavity-stabilized mode is dominant, while for larger inlet temperatures (case RFSC-HST), non-negligible water vapor dissociation and heat release occur in the vicinity of the fuel injection. These two modes are illustrated in Fig. 22, which presents an instantaneous snapshot at $t^* = 950.0$ of the iso-surface $\widetilde{\xi} = 0.5$ of the filtered fuel inlet tracer $\widetilde{\xi}$ (in light grey) as well as an isovalue of the OH filtered mass fraction $\widetilde{Y}_{\mathrm{OH}}$ colored by the normalized filtered temperature $\widetilde{T}/T_0$, for both simulated cases.

Whatever the leading mechanism of combustion stabilization, e.g., self-ignition or flame propagation phenomena, the temperature of the fresh mixture T_u appears as a critical parameter. Figure 23 presents filtered temperature scatterplots issued from the non-reactive flow simulations. It is plotted against the filtered mixture fraction $\widetilde{\xi}$ together with a standard linear approximation (dashed line) and a polynomial approximation (continuous line). The linear approximation is expressed thanks to the following expression $T_u\left(\xi\right) = \widetilde{\xi}\, T_{fuel} + \left(1 - \widetilde{\xi}\right) T_{ox}$ with T_{fuel} the hydrogen inlet stream temperature and T_{ox} the vitiated air inlet stream temperature, the values of which are provided in Table 1.

In fact, it must be emphasized that the use of a linear expression to express the temper-

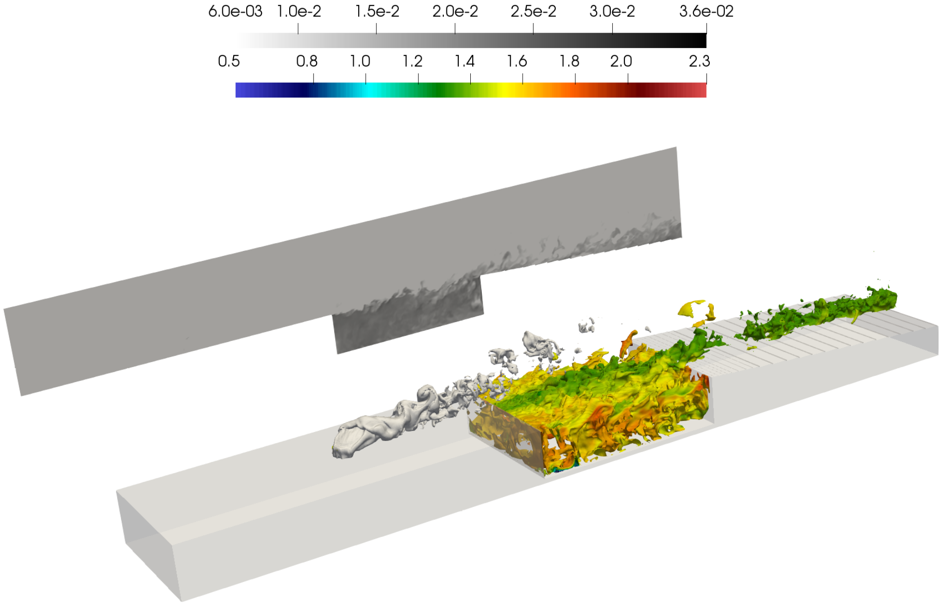

(a) case RFSC-LST

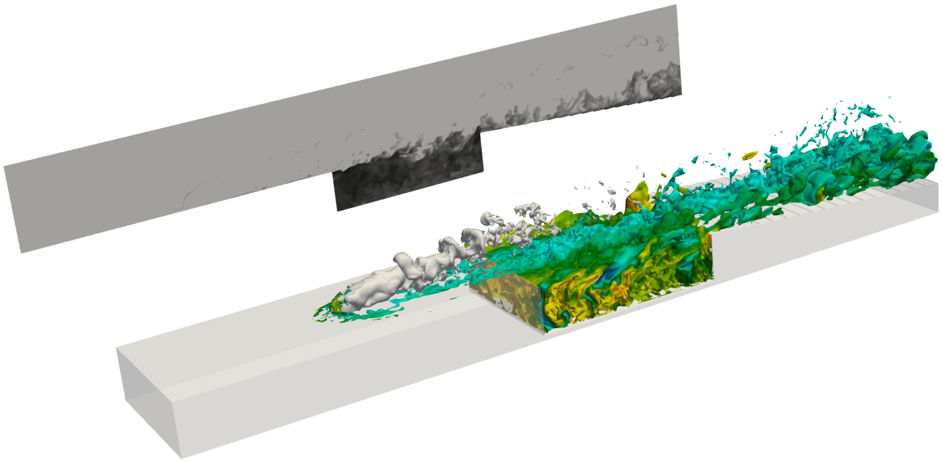

(b) case RFSC-HST

Figure 22: Isovalue surface of the OH filtered mass fraction colored by the normalized filtered temperature $\widetilde{T}/T_0$ and fuel inlet tracer iso-surface $\widetilde{\xi} = 0.5$. Back side: OH mass fraction. Top: grayscale levels associated to Y_{OH} variations, colormap associated to normalized temperature variations.

ature of the fresh mixture as a function of the mixture fraction is highly questionable. First, temperature is not an extensive quantity and, for such supersonic flow conditions, it would be more relevant to express the total enthalpy as a function of the mixture fraction (Mura and Izard, 2010). As previously emphasized by Izard et al. (2009), a linear relationship between total enthalpy and mixture fraction may hold if the Lewis and Prandt numbers are unity and the effects induced by temporal variations of pressure remains negligible. In addition to this, it seems worth recalling that, in supersonic flow regimes, compressibility effects may play an important role, in such a manner that the linear representation may no longer be adequate because of the presence of shock and expansion waves. In the present simulation, the fuel jet

($\widetilde{\xi} = 1$) strongly expands, causing a significant temperature decrease. The temperature then increases with the Mach disk compression, whereas the oxidizer stream ($\widetilde{\xi} = 0$) characteristics are altered through the bow shock compression and wall friction. Considering all these complex effects, which are difficult to include within a simple mathematical expression, it is proposed instead to fit the results of the non-reactive numerical simulation using a fourth-order polynomial approximation so as to express the temperature as a function of the mixture fraction. The corresponding evolution $T_u(\xi)$ is depicted in Fig. 23.

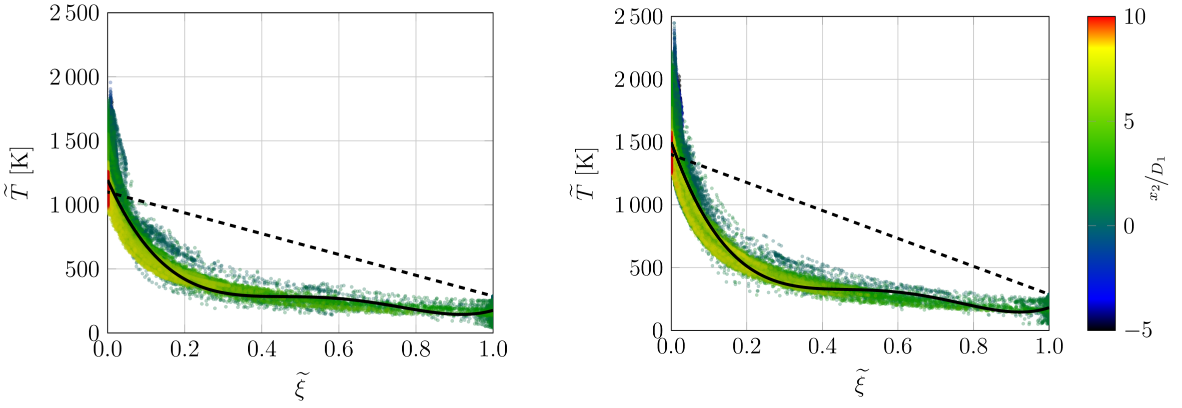

(a) case RFSC-LST

(b) case RFSC-HST

Figure 23: Scatterplots of the fresh reactant temperature

Since chemical reactions take place far downstream of the fuel injection, it seems worthwhile to attempt to discriminate between premixed and non-premixed (i.e. diffusive) combustion contributions. A premixedness index $\check{\zeta}_p$ is therefore considered. It is defined as follows:

$$\check{\zeta}_p = \frac{1}{2}\left(1 + \mathbf{n}_F \cdot \mathbf{n}_O\right) \tag{19}$$

with $\mathbf{n}_F$ and $\mathbf{n}_O$ being normal unit vectors associated to the direction of the molecular diffusion fluxes of the fuel and oxidizer, respectively, which are evaluated from $\mathbf{n}_F = \widetilde{\mathbf{V}}_F / \left\| \widetilde{\mathbf{V}}_F \right\|$ and $\mathbf{n}_O = \widetilde{\mathbf{V}}_O / \left\| \widetilde{\mathbf{V}}_O \right\|$ where $\widetilde{\mathbf{V}}_F$ and $\widetilde{\mathbf{V}}_O$ denote the filtered diffusion velocity of the fuel and oxidizer, respectively. As it is defined, this index is expected to approach zero for diffusive combustion and unity for premixed combustion. It should be fairly recognized that its representativity can be questioned in certain situations but it remains widely used in preliminary inspections of partially-premixed combustion (Martínez-Ferrer et al., 2017b). Figure 24 displays the PDF of this premixedness index obtained in a volume restricted to $0.01 \leq \widetilde{\xi} \leq 0.99$ at several times for cases RFSC-LST and RFSC-HST[4]. The peak associated to a premixedness index equal to zero is much higher than the peak associated to unity indicating mostly diffusive combustion. However, the contribution of the premixed mode to the HRR is more significant and corresponds to a premixed flame structure (in red) that develops in the vicinity of the cavity leading edge, as it can be seen in the top part of Fig. 24.

---

[4] Only the samples associated to non-negligible values of the HRR are considered

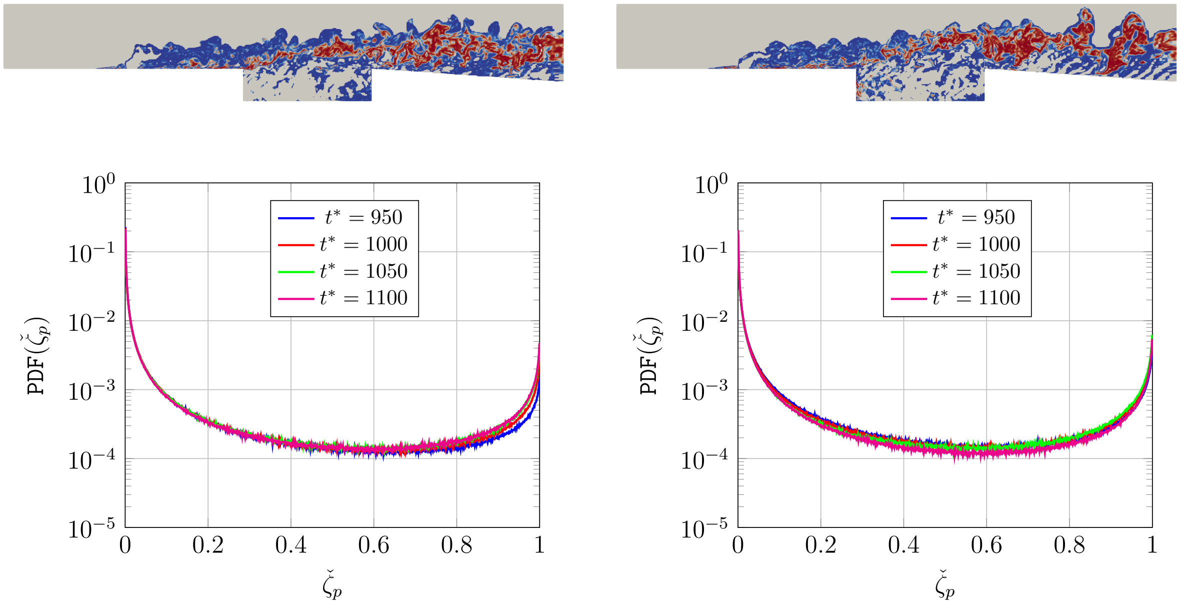

(a) case RFSC-LST

(b) case RFSC-HST

Figure 24: Premixedness index distribution: field in the median plane at time $t^* = 1100.0$ (top) and associated PDF at various times (bottom)

Since a non-negligible amount of chemical reaction takes place in a premixed combustion mode, attention is now focused on this contribution. To this purpose, some preliminary computations are performed with the `Cantera` software, considering mixtures of fresh reactants at various composition with the temperature of the fresh mixture set according to the polynomial expression $T_u(\xi)$ discussed above. The chemistry description used to perform this set of computations is the same as the one retained to perform the whole set of simulations. Figure 25 displays the self-ignition delay of the corresponding mixtures as a function of the mixture fraction (top) or equivalence ratio (bottom) for cases RFSC-LST and RFSC-HST. It is plotted together with the polynomial expression retained for the fresh reactant temperature.

From the obtained results, it is noteworthy that, as the mixture fraction is increased from the left to the right side of Fig. 25, the self-ignition delay first decreases and displays a local minimum for the most reactive conditions ξ_{mr} and then increases, until it reaches very large values for rich mixtures. As expected, the most reactive state, which corresponds to a minimal value of the self-ignition delay, does not correspond to stoichiometry. This is a direct outcome of the vitiation of the oxidizer inlet stream, which features a temperature that is significantly larger than the one of the fuel inlet stream. It is also remarkable that the self-ignition delay displays a sharp increase for rich conditions, in such a manner that spontaneous ignition regimes are less likely for these mixtures. More precisely, the corresponding auto-ignition regimes require more time to develop, which may favor premixed flame propagation. We will see below that the characteristic time scales of premixed flame propagation indeed remain significantly smaller than the ignition delays for such rich mixtures. However, as long as lean conditions are considered, only the auto-ignition regimes are expected to occur.

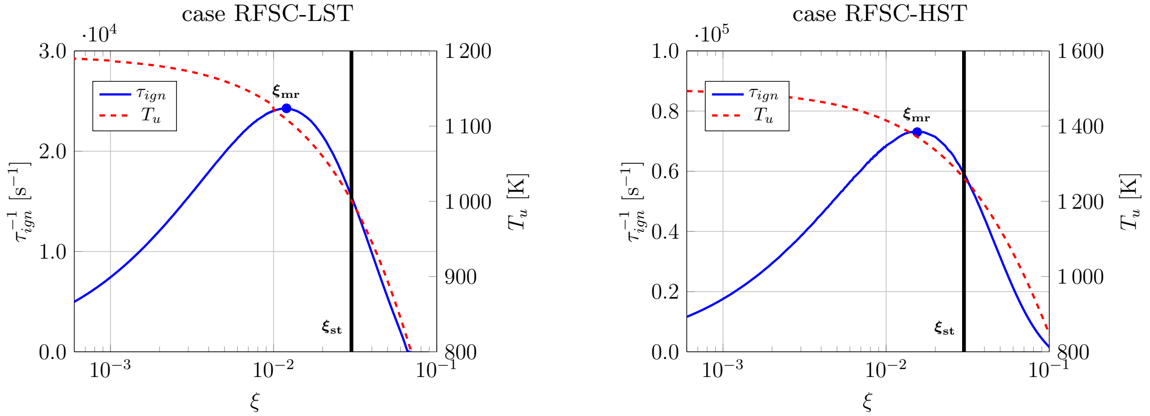

Figure 25: Self-ignition delay τ_{ign} as a function of the mixture fraction

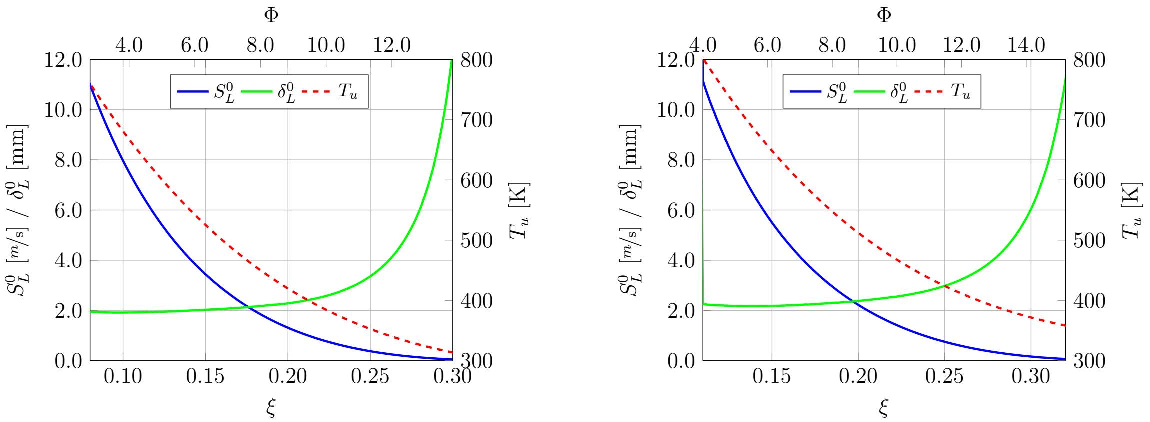

(a) case RFSC-LST

(b) case RFSC-HST

Figure 26: Laminar flame velocity S_L^0 and thickness δ_L^0 as functions of the mixture fraction

Figure 26 displays the evolution of the laminar premixed flame velocity S_L^0 and associated flame thickness δ_L^0 computed again with the detailed chemical mechanism of O'Conaire et al. (2004). In this figure, for both conditions (RFSC-LST and RFSC-HST), the left boundary of the depicted mixture fraction range corresponds to the value below which flame propagation is no longer relevant. Indeed, below this value, it becomes impossible to perform the premixed flame computation because self-ignition may occur. For such values of the mixture fraction, the computations thus displays an exacerbated sensitivity to numerical simulation parameters including the length of the computational domain, the number of computational nodes, the choice of the integration time step, etc. This is in constrast to the right boundary of the mixture fraction domain beyond which the laminar flame propagation velocity tends to zero; it corresponds to the high flammability limit. In this respect, the figure shows that, as S_L^0 decreases, the flame thickness δ_L^0 increases also, up to the flammability limit. The associated flame propagation time scale or flame transit time, defined as $\tau_L^0 = \delta_L^0 / S_L^0$, is displayed as a function of the mixture fraction in Fig. 27. In a restricted mixture fraction domain bounded by the two limits discussed above, the laminar premixed flame velocity S_L^0 (resp. the transit time scale τ_L^0) decreases (resp. increases) with the mixture fraction, as it is shown in Figs. 26

and 27. The laminar premixed flame velocity should reach a maximum in the vicinity of the stoichiometry but, as emphasized above, the self-ignition mechanism is the leading order phenomenom for these compositions of the reactive mixture.

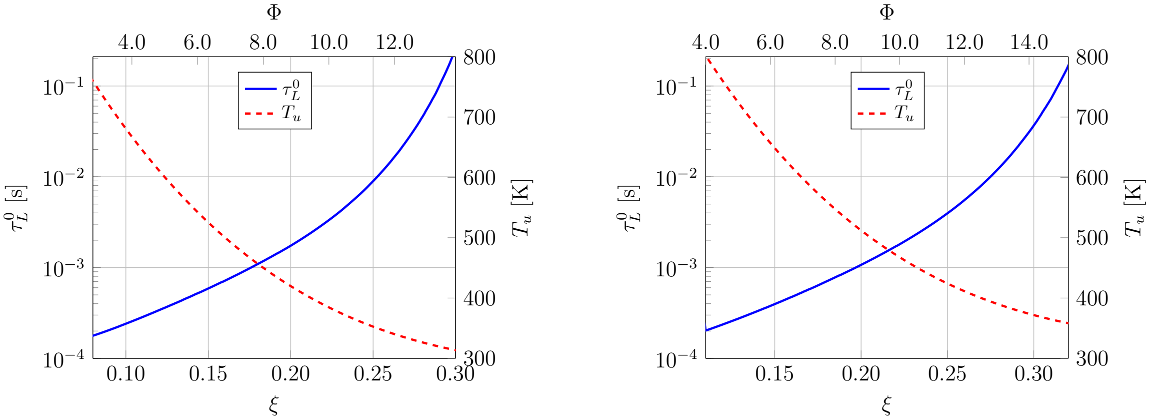

(a) case RFSC-LST

(b) case RFSC-HST

Figure 27: Flame propagation timescale τ_L^0 as a function of the mixture fraction

Turbulent premixed combustion regimes are now analyzed using the coordinates introduced by Barrère and Borghi (Borghi, 1984, 1985). The data are thus plotted in Fig. 28 using a normalized length scale ratio ℓ_t/δ_L^0 and velocity ratio u_{rms}/S_L^0 as the set of coordinates. In these expressions, the turbulence integral length scale is approximated from $\ell_t = u_{rms}^3/\varepsilon$ with ε the resolved molecular dissipation rate, which has been evaluated as the trace of the second rank resolved molecular dissipation rate tensor, i.e.,

$$\varepsilon_{ij} = \frac{1}{\langle \rho \rangle} \left\langle \left(\overline{\tau}_{ik} - \langle \overline{\tau}_{ik} \rangle\right) \frac{\partial}{\partial x_k} \left(\frac{\overline{\rho}\widetilde{u}_j - \langle \overline{\rho}\widetilde{u}_j \rangle}{\langle \rho \rangle} \right) + \left(\overline{\tau}_{jk} - \langle \overline{\tau}_{jk} \rangle\right) \frac{\partial}{\partial x_k} \left(\frac{\overline{\rho}\widetilde{u}_i - \langle \overline{\rho}\widetilde{u}_i \rangle}{\langle \rho \rangle} \right) \right\rangle \quad (20)$$

The velocity fluctuation RMS is approximated from $u_{rms} = \sqrt{2k/3}$ with k the resolved turbulent kinetic energy, which is evaluated from $k = \left(\langle \overline{\rho}\widetilde{u}_i\widetilde{u}_i \rangle - \langle \overline{\rho} \rangle \langle \widetilde{u}_i \rangle \langle \widetilde{u}_i \rangle\right) / (2 \langle \overline{\rho} \rangle)$. The flame characteristics are estimated from the local conditions associated to the corresponding unburnt mixtures. Quantities S_L^0 and δ_L^0 are thus computed at each computational point that fulfills the following two conditions: (i) the mixture fraction remains within the lean and rich flammability limits, i.e., within a range where premixed flame propagation may occur, and (ii) the considered point lies inside a zone where the probability to obtain a premixed flame structure remains larger than a given threshold value, which is presently set to 40%.

Figure 28 shows that, from one location to another, the turbulent combustion regimes are highly variable. Some points correspond to quasi-laminar conditions, while others feature strong turbulence-chemistry interactions (TCI). It should be emphasized that, with thick flames, thickened-wrinkled flames, and even laminar ones, almost all possible turbulent combustion regimes may be found. In condition RFSC-LST, most of the points are located in the vicinity of thickened-wrinkled flame regime, between the line Da = 1.0 and the Klimov-

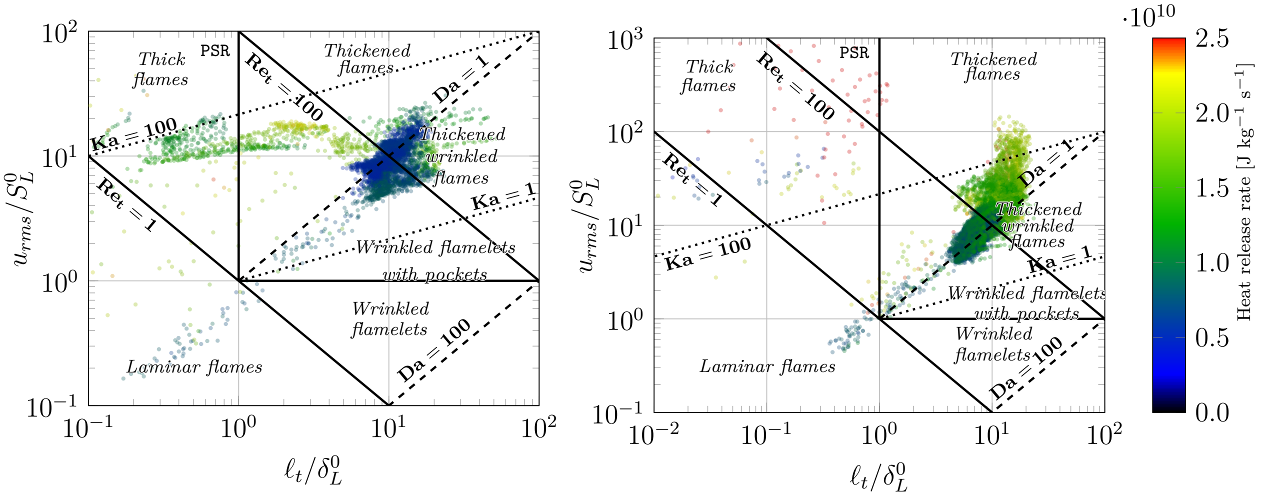

(a) case RFSC-LST

(b) case RFSC-HST

Figure 28: Premixed turbulent combustion diagram based on the Borghi-Barrère coordinates (Borghi, 1985)

Williams limit[5] (Williams, 1976), around the horizontal line corresponding to $u_{rms}/S_L^0 = 10.0$. These regimes are consistent with those previously reported by Quinlan et al. (2014) for scramjet conditions. There are also some points featuring a non-negligible heat release rate located in the thick flame region. It is noteworthy that the corresponding points are located in the vicinity of the hydrogen injection, where the reactive mixture remains highly segregated and velocity fluctuations are quite large. On average, the case RFSC-HST displays significantly larger heat release rates, with a statistics spread towards the thickened and thickened-wrinkled flame regimes, which corresponds to smaller values of the Damköhler number. Also, chemical reactions take place at locations where velocity fluctuations may reach extremely large values and, as a consequence, non-negligible finite-rate chemistry effects come into play.

It is noteworthy that the above evaluation of the dissipation rate ε does not account for the unresolved (i.e., modelled) contribution. The relevance of this approximation can be evaluated through a complementary analysis of the computational results. The objective of this analysis is to provide an additional assessment of the LES resolution level by investigating the contribution of the SGS model to the turbulent energy dissipation. To quantify the SGS contribution, one can define two components $\varepsilon_{\langle \mathsf{SGS} \rangle}$ and $\varepsilon'_{\mathsf{SGS}}$, which are acting on the resolved turbulent kinetic energy and SGS turbulent kinetic energy $\langle k_{\mathsf{SGS}} \rangle$, see for instance Ben-Nasr et al. (2017). Following Davidson (2006), these two components can be formulated in such a manner that

$$\varepsilon_{\mathsf{SGS}} = \varepsilon_{\langle \mathsf{SGS} \rangle} + \varepsilon'_{\mathsf{SGS}} \tag{21}$$

where the two contributions are evaluated from

$$\varepsilon_{\langle \mathsf{SGS} \rangle} = \frac{1}{\langle \rho \rangle} \left\langle T^*_{ij} \right\rangle \frac{\partial \left\langle \widetilde{u}_j \right\rangle}{\partial x_k} \tag{22}$$

---

[5] It may be worthwhile to recall that this limit corresponds to Ka = 1.0.

and

$$\varepsilon'_{\mathtt{SGS}} = \frac{1}{\langle\rho\rangle}\left\langle \left(T^*_{ij} - \left\langle T^*_{ij}\right\rangle\right)\frac{\partial}{\partial x_k}\left(\frac{\overline{\rho}\widetilde{u}_j - \langle\overline{\rho}\widetilde{u}_j\rangle}{\langle\rho\rangle}\right)\right\rangle \tag{23}$$

with T^*_{ij} the deviatoric part of the subgrid-scale (SGS) stress tensor T_{ij}.

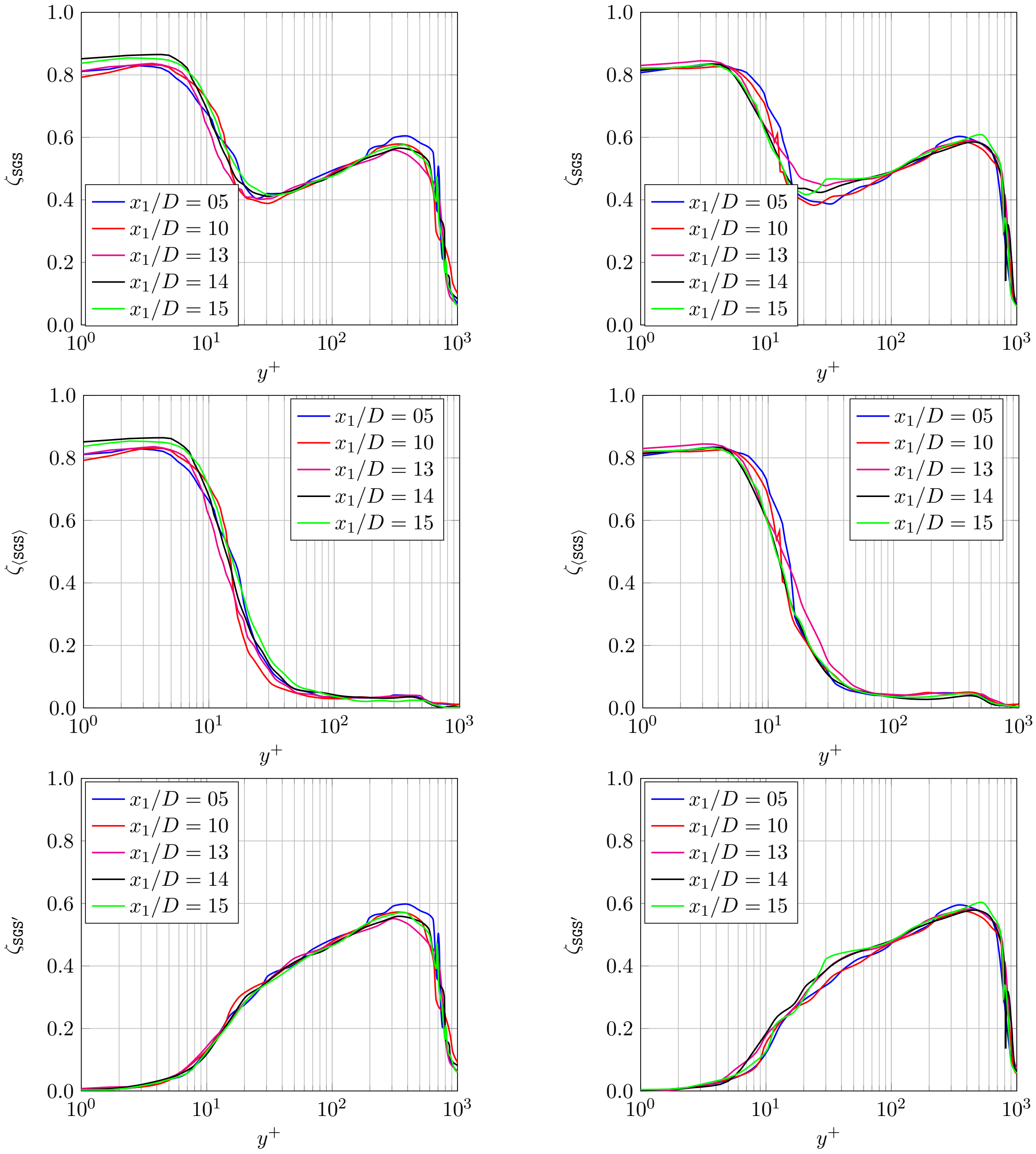

(a) case RFSC-LST

(b) case RFSC-HST

Figure 29: SGS Activity parameters as functions of y^+

As defined above, the total SGS dissipation of a LES model, $\varepsilon_{\mathtt{SGS}}$, is the sum of both the SGS dissipation associated to the average of the filtered flowfield, $\varepsilon_{\langle\mathtt{SGS}\rangle}$, and the one due to the fluctuating flowfield, $\varepsilon'_{\mathtt{SGS}}$. Thus, a global SGS activity parameter can be defined as:

$$\zeta_{\mathtt{SGS}} = \frac{\varepsilon_{\mathtt{SGS}}}{\varepsilon_{\mathtt{SGS}} + \varepsilon} \tag{24}$$

while the activities due to the averaged and fluctuating flowfield can be discriminated by considering instead

$$\zeta_{\langle \mathtt{SGS} \rangle} = \frac{\varepsilon_{\langle \mathtt{SGS} \rangle}}{\varepsilon_{\langle \mathtt{SGS} \rangle} + \varepsilon} \tag{25}$$

and

$$\zeta'_{\mathtt{SGS}} = \frac{\varepsilon'_{\mathtt{SGS}}}{\varepsilon'_{\mathtt{SGS}} + \varepsilon} \tag{26}$$

These three indexes are reported in Fig. 29. This figure displays the SGS activity parameter $\zeta_{\mathtt{SGS}}$, together with its two components $\zeta_{\langle \mathtt{SGS} \rangle}$ and $\zeta'_{\mathtt{SGS}}$, as functions of y^+ at different cross-stream locations. In the viscous sublayer and up to $y^+ = 5$, the value of the SGS activity parameter $\zeta_{\mathtt{SGS}}$ (top of Fig. 29) is approximately equal to 0.8. In the transition region and up to $y^+ = 300$, it decreases and reaches a minimum of 0.4 at $y^+ = 20$, $\zeta_{\mathtt{SGS}}$ increases in the outer region of the boundary layer and reaches a maximum value of about 0.6, to decrease again at the edge of the boundary layer. The SGS activity parameter $\zeta_{\langle \mathtt{SGS} \rangle}$ associated to the filtered-averaged flowfield (middle of Fig. 29) confirms that the SGS dissipation is mainly driven by viscous effects in the near-wall region, while the fluctuating velocity field is dominant in the transition and outer regions. Not only the behaviour but also the values reported above are fully consistent with the results previously obtained with the WALE subgrid-scale closure by Ben-Nasr et al. (2017).

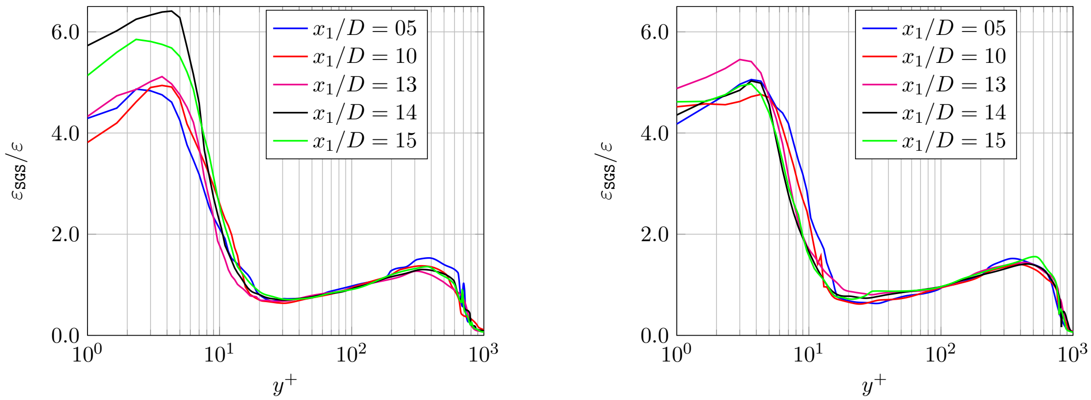

(a) case RFSC-LST

(b) case RFSC-HST

Figure 30: Ratio of the SGS dissipation to the viscous dissipation, i.e., $\varepsilon_{\mathtt{SGS}}/\varepsilon$, as a function of y^+

Finally, the ratio of the SGS dissipation $\varepsilon_{\mathtt{SGS}}$ to the resolved viscous dissipation $\varepsilon_{\mathtt{SGS}}$ is plotted as a function of y^+ in Fig. 30. It is remarkable that, in a wide range of the boundary layer, from about $y^+ = 15$ to $y^+ = 200$, this ratio takes values smaller than unity and, even at larger distances from the wall, it does exceed 1.5. This confirms that the resolved dissipation rate ε, as given by Eq. 20, provides a rather satisfactory estimate of the TKE dissipation rate, which can be used to evaluate characteristic turbulence scales so as to proceed with a qualitative inspection of turbulent combustion regimes.

6. Summary and conclusions

A new set of highly-resolved large-eddy simulations is presented. It corresponds to the geometry of a jet in a supersonic crossflow (JISCF) of vitiated air delivering hydrogen upstream of a squared cavity. The conditions are relevant to experiments previously conducted at the University of Michigan. To the best of the authors' knowledge, this is the first detailed computational investigation of this experimental test case. The computations are performed with the computational solver `CREAMS` and make use of a recent immersed boundary method (IBM) algorithm. The wall-adapting local eddy (WALE) model is retained as the subgrid-scale viscosity closure. Several criteria are used to check the computational resolution, especially near the walls, which are represented through an IBM, where some efforts have been spent to capture the flow as accurately as possible. The use of the WALE model allows to satisfactorily recover the behavior in the buffer layer that separates the logarithmic zone from the viscous sublayer. The filtered chemical rates are represented using either the PSR or the U-PaSR closures and it is remarkable that, for the present level of computational resolution, the results obtained using the two distinct frameworks are very similar.

Depending on the inlet vitiated airstream temperature, two stabilization modes are recovered: cavity-stabilized regime and jet-wake stabilized regime. In the cavity-stabilized combustion mode, combustion is anchored at the leading edge of the wall-mounted cavity and spreads into the main flow at an approximately constant angle, whereas jet-wake stabilized combustion takes place directly downstream of the fuel injection, i.e., upstream of the cavity. In this respect, it seems worth mentioning that different averaged streamline flowfields – not reported for the sake of conciseness – have been obtained for cavity and jet-wake stabilization modes. For high operative temperatures, combustion primarily takes place in the jet-wake stabilization mode while, for lower operative temperatures, the cavity stabilization mode is obtained. This is consistent with the experimental results of Micka and Driscoll (2008). In this respect, the present set of computations constructively complements the experimental data, e.g., the corresponding computational data are used to discriminate the contributions of premixed and non-premixed combustion modes. The turbulent combustion regimes are also inspected on the basis of classical combustion diagrams for the two levels of inlet temperature that have been considered. This analysis confirms the occurrence of highly turbulent premixed flame conditions. For intermediate values of the operative temperature, some oscillations between the two modes are expected and it would be interesting to run complementary numerical simulations at these intermediate operative temperatures so as to understand how these oscillations may happen and how long each stabilization mode is active. This offers an interesting perspective for future works.

7. Acknowledgments

This study is a part of the Ph.D. Thesis of F.H. Eugênio Ribeiro, which is financially supported by the Brazilian program Ciência sem Fronteiras of CNPq and Brazilian Air Force.

F.H. Eugênio Ribeiro is indebted to Dr. Anthony Techer and Aimad Er-Raiy for many stimulating discussions on tricky technical issues. This work was granted access to the HPC resources of CINES, IDRIS, and TGCC under the allocations x20152b7456 and i20152b7251. A part of this work has been presented during the invited plenary talk entitled "High-fidelity numerical simulation of reactive high-speed flows" given by Arnaud Mura at the tenth International Conference on Computational Fluid Dynamics (ICCFD10) held in Barcelona (Spain).

References

Anderson, J. D. (1989). *Hypersonic and high temperature temperature gas dynamics*. McGraw-Hill.

Ben-Nasr, O., Hadjadj, A., Chaudhuri, A., and Shadloo, M. (2017). Assessment of subgrid-scale modeling for large-eddy simulation of a spatially-evolving compressible turbulent boundary layer. *Computers & Fluids*, 151:144–158.

Ben Yakar, A. and Hanson, R. K. (1998). Experimental investigation of flame-holding capability of hydrogen transverse jet in supersonic cross-flow. *Symposium (International) on Combustion*, 27:2173–2180.

Ben-Yakar, A. and Hanson, R. K. (2001). Cavity flame-holders for ignition and flame stabilization in scramjets: an overview. *Journal of Propulsion and Power*, 17(4):869–877.

Berglund, M., Fedina, E., Fureby, C., Tegner, J., and Sabelnikov, V. A. (2010). Finite rate chemistry large-eddy simulation of self-ignition in supersonic combustion ramjet. *AIAA Journal*, 48(3):540–550.

Borghi, R. (1984). Sur la structure des flammes turbulentes. *Journal de Chimie Physique*, 81:361–370.

Borghi, R. (1985). On the structure and morphology of turbulent premixed flames. In *Recent advances in the Aerospace Sciences*, pages 117–138. Springer.

Boukharfane, R., Ribeiro, F. H. E., Bouali, Z., and Mura, A. (2018). A combined ghost-point-forcing/direct-forcing immersed boundary method (IBM) for compressible flow simulations. *Computers & Fluids*, 162:91–112.

Buttay, R., Gomet, L., Lehnasch, G., and Mura, A. (2017). Highly resolved numerical simulation of combustion downstream of a rocket engine igniter. *Shock Waves*, 27(4):655–674.

Buttay, R., Lehnasch, G., and Mura, A. (2016). Analysis of small-scale scalar mixing processes in highly under-expanded jets. *Shock Waves*, 26(2):193–212.

Cai, Z., Liu, X., Gong, C., Sun, M., Wang, Z., and Bai, X. S. (2016). Large-eddy simulation of the fuel transport and mixing process in a scramjet combustor with rearwall-expansion cavity. *Acta Astronautica*, 126:375–381.

Cai, Z., Zhu, J., Sun, M., Wang, Z., and Bai, X. S. (2018). Ignition processes and modes excited by laser-induced plasma in a cavity-based supersonic combustor. *Applied Energy*, 228:1777–1782.

Candler, G. V., Cymbalist, N., and Dimotakis, P. E. (2017). Wall-modeled large-eddy simulation of autoignition-dominated supersonic combustion. *AIAA Journal*, 55(7):2410–2423.

Celik, I., Cehreli, Z., and Yavuz, I. (2005). Index of resolution quality for large eddy simulations. *Journal of Fluids Engineering*, 127(5):949–958.

Daly, B. and Harlow, F. (1970). Transport equations in turbulence. *The Physics of Fluids*, 13(11):2634–2649.

Davidson, L. (2006). Transport equations in incom- pressible urans and les. Technical report, Chalmers University of Technology Report 2006/01.

Dubois, T., Domaradzki, J. A., and Honein, A. (2002). The subgrid-scale estimation model applied to large eddy simulations of compressible turbulence. *Physics of Fluids*, 14(5):1781–1801.

Ertesvag, I. S. and Magnussen, B. F. (2000). The eddy dissipation turbulence energy cascade model. *Combustion Science and Technology*, 159(1):213–235.

Fulton, J. A., Edwards, J. R., Cutler, A., McDaniel, J., and Goyne, C. (2016). Turbulence/chemistry interactions in a ramp-stabilized supersonic hydrogen-air diffusion flame. *Combustion and Flame*, 174:152–165.

Garnier, E., Adams, N., and Sagaut, P. (2009). *Large eddy simulation for compressible flows.* Springer.

Gomet, L., Robin, V., and Mura, A. (2012). Influence of residence and scalar mixing time scales in non-premixed combustion in supersonic turbulent flows. *Combustion Science and Technology*, 184(10-11):1471–1501.

Gomet, L., Robin, V., and Mura, A. (2015). A multiple-inlet mixture fraction model for nonpremixed combustion. *Combustion and Flame*, 162(3):668–687.

Gong, C., Jangi, M., Bai, X. S., Liang, J. H., and Sun, M. (2017). Large-eddy simulation of hydrogen combustion in supersonic flows using an eulerian stochastic fields method. *International Journal of Hydrogen Energy*, 42(2):1264–1275.

Gruber, M. R., Donbar, J. M., Carter, C. D., and Hsu, K.-Y. (2004). Mixing and combustion studies using cavity-based flameholders in a supersonic flow. *Journal of Propulsion and Power*, 20(5):769–778.

Heiser, W. H. and Pratt, D. T. (1994). *Hypersonic airbreathing propulsion.* AIAA Education Series.

Hirschfelder, J. and Curtiss, C. (1949). The theory of flame propagation. *The Journal of Chemical Physics*, 17(11):1076–1081.

Izard, J. F., Lehnasch, G., and Mura, A. (2009). A Lagrangian model of combustion in high-speed flows: application to scramjet conditions. *Combustion Science and Technology*, 181(11):1372–1396.

Kawai and Lele (2010). Large-eddy simulation of jet mixing in supersonic crossflows. *AIAA Journal*, 48(9):2063–2083.

Kline, S. J., Reynolds, W. C., Schraub, F., and Runstadler, P. (1967). The structure of turbulent boundary layers. *Journal of Fluid Mechanics*, 30(4):741–773.

Kosovic, B., Pullin, D. I., and Samtaney, R. (2002). Subgrid-scale modeling for large-eddy simulations of compressible turbulence. *Physics of Fluids*, 14(4):1511–1522.

Lawson, S. and Barakos, G. (2011). Review of numerical simulations for high-speed, turbulent cavity flows. *Progress in Aerospace Sciences*, 47(3):186–216.

Lesieur, M., Métais, O., and Comte, P. (2005). *Large-eddy simulations of turbulence*. Cambridge University Press.

Liu, C., Zhao, Y., Wang, Z., Wang, H., and Sun, M. (2017). Dynamics and mixing mechanism of transverse jet injection into a supersonic combustor with cavity flameholder. *Acta Astronautica*, 136:90–100.

Martínez-Ferrer, P. J., Buttay, R., Lehnasch, G., and Mura, A. (2014). A detailed verification procedure for compressible reactive multicomponent Navier–Stokes solvers. *Computers & Fluids*, 89:88–110.

Martínez-Ferrer, P. J., Lehnasch, G., and Mura, A. (2017a). Compressibility and heat release effects in high-speed reactive mixing layers: growth rates and turbulence characteristics. *Combustion and Flame*, 180:284–303.

Martínez-Ferrer, P. J., Lehnasch, G., and Mura, A. (2017b). Compressibility and heat release effects in high-speed reactive mixing layers: structure of the stabilization zone and modeling issues relevant to turbulent combustion in supersonic flows. *Combustion and Flame*, 180:304–320.

Mathur, T., Gruber, M., Jackson, K., Donbar, J., Donaldson, W., Jackson, T., and Billig, F. (2001). Supersonic combustion experiments with a cavity-based fuel injector. *Journal of Propulsion and Power*, 17(6):1305–1312.

Micka, D. (2010). *Combustion stabilization, structure, and spreading in a laboratory dual-mode scramjet combustor*. PhD thesis, University of Michigan.

Micka, D. and Driscoll, J. (2008). Dual-mode combustion of a jet in cross-flow with cavity flameholder. *AIAA Paper 2008-1062*.

Micka, D. J. and Driscoll, J. F. (2009). Combustion characteristics of a dual-mode scramjet combustor with cavity flameholder. *Proceedings of the Combustion Institute*, 32(2):2397–2404.

Moule, Y., Sabelnikov, V. A., and Mura, A. (2014a). Highly resolved numerical simulation of combustion in supersonic hydrogen–air coflowing jets. *Combustion and Flame*, 161(10):2647–2668.

Moule, Y., Sabelnikov, V. A., Mura, A., and Smart, M. (2014b). Computational fluid dynamics investigation of a Mach 12 scramjet engine. *Journal of Propulsion and Power*, 30(2):461–473.

Mura, A. and Izard, J. F. (2010). Numerical simulation of supersonic nonpremixed turbulent combustion in a scramjet combustor model. *Journal of Propulsion and Power*, 26(4):858–868.

Nicoud, F. and Ducros, F. (1999). Subgrid-scale stress modelling based on the square of the velocity gradient tensor. *Flow, Turbulence and Combustion*, 62(3):183–200.

O'Conaire, M., Curran, H. J., Simmie, J. M., Pitz, W. J., and Westbrook, C. K. (2004). A comprehensive modeling study of hydrogen oxidation. *International Journal of Chemical Kinetics*, 36(11):603–622.

Peters, N. (2000). *Turbulent Combustion.* Cambridge University Press.

Piomelli, U. (1999). Large-eddy simulation: achievements and challenges. *Progress in Aerospace Sciences*, 35(4):335–362.

Piomelli, U. and Balaras, E. (2002). Wall-layer models for large-eddy simulations. *Annual Review of Fluid Mechanics*, 34(1):349–374.

Piomelli, U. and Chasnov, J. R. (1996). Large-eddy simulations: theory and applications. In *Turbulence and Transition Modelling*, pages 269–336. Springer.

Pope, S. B. (2000). *Turbulent flows.* Cambridge University Press.

Pope, S. B. (2004). Ten questions concerning the large-eddy simulation of turbulent flows. *New Journal of Physics*, 6(1). p. 35.

Potturi, A. and Edwards, J. R. (2015). Large-eddy/Reynolds-averaged Navier-Stokes simulation of cavity-stabilized ethylene combustion. *Combustion and Flame*, 162(4):1176–1192.

Quinlan, J., McDaniel, J. C., Drozda, T. G., Lacaze, G., and Oefelein, J. C. (2014). A priori analysis of flamelet-based modeling for a dual-mode scramjet combustor. *AIAA Paper 2014–3743.*

Ragab, S. A., Sheen, S.-C., and Sreedhar, M. (1992). An investigation of finite-difference methods for large-eddy simulation of a mixing layer. *AIAA Paper 92-0554.*

Segal, C. (2009). *The scramjet engine: processes and characteristics*. Cambridge University Press.

Smart, M. and Tetlow, M. (2009). Orbital delivery of small payloads using hypersonic air-breathing propulsion. *Journal of Spacecraft and Rockets*, 46(1):117–125.

Smart, M. K. (2008). Scramjets. Technical report, RTO-EN-AVT-150-09.

Sun, M., Geng, H., Liang, J. H., and Wang, Z. G. (2008). Flame characteristics in supersonic combustor with hydrogen injection upstream of cavity flameholder. *Journal of Propulsion and Power*, 24(4):688–696.

Techer, A., Moule, Y., Lehnasch, G., and Mura, A. (2018). Mixing of fuel jet in supersonic crossflow: estimation of subgrid-scale scalar fluctuations. *AIAA Journal*, 56(2):465–481.

Urzay, J. (2018). Supersonic combustion in air-breathing propulsion systems for hypersonic flight. *Annual Review of Fluid Mechanics*, 50:593–627.

Vedovoto, J., Silveira Neto, A., Figueira da Silva, L. F., and Mura, A. (2015). Influence of synthetic inlet turbulence on the prediction of low mach number flows. *Computers & Fluids*, 106:135–153.

Williams, F. A. (1976). Criteria for existence of wrinkled laminar flame structure of turbulent premixed flames. *Combustion and Flame*, 26:269–270.

Yoshizawa, A. (1986). Statistical theory for compressible turbulent shear flows, with the application to subgrid modeling. *Physics of Fluids*, 29(7):2152–2164.

Zabetakis, M. G. (1965). Flammability characteristics of combustible gases and vapors. Technical report, Bureau of Mines, Washington DC.

Zettervall, N. and Fureby, C. (2018). A computational study of ramjet, scramjet and dual-mode ramjet combustion in combustor with a cavity flameholder. *AIAA 2018-1146*.